

Production of ϕ mesons at mid-rapidity in $\sqrt{s_{NN}} = 200$ GeV Au+Au collisions at RHIC

S.S. Adler,⁵ S. Afanasiev,¹⁷ C. Aidala,⁵ N.N. Ajitanand,⁴³ Y. Akiba,^{20,38} J. Alexander,⁴³ R. Amirikas,¹² L. Aphecetche,⁴⁵ S.H. Aronson,⁵ R. Auerbeck,⁴⁴ T.C. Awes,³⁵ R. Azmoun,⁴⁴ V. Babintsev,¹⁵ A. Baldissieri,¹⁰ K.N. Barish,⁶ P.D. Barnes,²⁷ B. Bassalleck,³³ S. Bathe,³⁰ S. Batsouli,⁹ V. Baublis,³⁷ A. Bazilevsky,^{39,15} S. Belikov,^{16,15} Y. Berdnikov,⁴⁰ S. Bhagavatula,¹⁶ J.G. Boissevain,²⁷ H. Borel,¹⁰ S. Borenstein,²⁵ M.L. Brooks,²⁷ D.S. Brown,³⁴ N. Bruner,³³ D. Bucher,³⁰ H. Buesching,³⁰ V. Bumazhnov,¹⁵ G. Bunce,^{5,39} J.M. Burward-Hoy,^{26,44} S. Butsyk,⁴⁴ X. Camard,⁴⁵ J.-S. Chai,¹⁸ P. Chand,⁴ W.C. Chang,² S. Chernichenko,¹⁵ C.Y. Chi,⁹ J. Chiba,²⁰ M. Chiu,⁹ I.J. Choi,⁵² J. Choi,¹⁹ R.K. Choudhury,⁴ T. Chujo,⁵ V. Cianciolo,³⁵ Y. Cobigo,¹⁰ B.A. Cole,⁹ P. Constantin,¹⁶ D.G. d'Enterria,⁴⁵ G. David,⁵ H. Delagrange,⁴⁵ A. Denisov,¹⁵ A. Deshpande,³⁹ E.J. Desmond,⁵ O. Dietzsch,⁴¹ O. Drapier,²⁵ A. Drees,⁴⁴ R. du Rietz,²⁹ A. Durum,¹⁵ D. Dutta,⁴ Y.V. Efremenko,³⁵ K. El Chenawi,⁴⁹ A. Enokizono,¹⁴ H. En'yo,^{38,39} S. Esumi,⁴⁸ L. Ewell,⁵ D.E. Fields,^{33,39} F. Fleuret,²⁵ S.L. Fokin,²³ B.D. Fox,³⁹ Z. Fraenkel,⁵¹ J.E. Frantz,⁹ A. Franz,⁵ A.D. Frawley,¹² S.-Y. Fung,⁶ S. Garpman,^{29,*} T.K. Ghosh,⁴⁹ A. Glenn,⁴⁶ G. Gogiberidze,⁴⁶ M. Gonin,²⁵ J. Gosset,¹⁰ Y. Goto,³⁹ R. Granier de Cassagnac,²⁵ N. Grau,¹⁶ S.V. Greene,⁴⁹ M. Grosse Perdekamp,³⁹ W. Guryn,⁵ H.-Å. Gustafsson,²⁹ T. Hachiya,¹⁴ J.S. Haggerty,⁵ H. Hamagaki,⁸ A.G. Hansen,²⁷ E.P. Hartouni,²⁶ M. Harvey,⁵ R. Hayano,⁸ X. He,¹³ M. Heffner,²⁶ T.K. Hemmick,⁴⁴ J.M. Heuser,⁴⁴ M. Hibino,⁵⁰ J.C. Hill,¹⁶ W. Holzmann,⁴³ K. Homma,¹⁴ B. Hong,²² A. Hoover,³⁴ T. Ichihara,^{38,39} V.V. Ikonnikov,²³ K. Imai,^{24,38} D. Isenhower,¹ M. Ishihara,³⁸ M. Issah,⁴³ A. Isupov,¹⁷ B.V. Jacak,⁴⁴ W.Y. Jang,²² Y. Jeong,¹⁹ J. Jia,⁴⁴ O. Jinnouchi,³⁸ B.M. Johnson,⁵ S.C. Johnson,²⁶ K.S. Joo,³¹ D. Jouan,³⁶ S. Kametani,^{8,50} N. Kamihara,^{47,38} J.H. Kang,⁵² S.S. Kapoor,⁴ K. Katou,⁵⁰ S. Kelly,⁹ B. Khachaturov,⁵¹ A. Khanzadeev,³⁷ J. Kikuchi,⁵⁰ D.H. Kim,³¹ D.J. Kim,⁵² D.W. Kim,¹⁹ E. Kim,⁴² G.-B. Kim,²⁵ H.J. Kim,⁵² E. Kistenev,⁵ A. Kiyomichi,⁴⁸ K. Kiyoyama,³² C. Klein-Boesing,³⁰ H. Kobayashi,^{38,39} L. Kochenda,³⁷ V. Kochetkov,¹⁵ D. Koehler,³³ T. Kohama,¹⁴ M. Kopytine,⁴⁴ D. Korchetkov,⁶ A. Kozlov,⁵¹ P.J. Kroon,⁵ C.H. Kuberg,^{1,27} K. Kurita,³⁹ Y. Kuroki,⁴⁸ M.J. Kweon,²² Y. Kwon,⁵² G.S. Kyle,³⁴ R. Lacey,⁴³ V. Ladygin,¹⁷ J.G. Lajoie,¹⁶ A. Lebedev,^{16,23} S. Leckey,⁴⁴ D.M. Lee,²⁷ S. Lee,¹⁹ M.J. Leitch,²⁷ X.H. Li,⁶ H. Lim,⁴² A. Litvinenko,¹⁷ M.X. Liu,²⁷ Y. Liu,³⁶ C.F. Maguire,⁴⁹ Y.I. Makdisi,⁵ A. Malakhov,¹⁷ V.I. Manko,²³ Y. Mao,^{7,38} G. Martinez,⁴⁵ M.D. Marx,⁴⁴ H. Masui,⁴⁸ F. Matathias,⁴⁴ T. Matsumoto,^{8,50} P.L. McGaughey,²⁷ E. Melnikov,¹⁵ F. Messer,⁴⁴ Y. Miake,⁴⁸ J. Milan,⁴³ T.E. Miller,⁴⁹ A. Milov,^{44,51} S. Mioduszewski,⁵ R.E. Mischke,²⁷ G.C. Mishra,¹³ J.T. Mitchell,⁵ A.K. Mohanty,⁴ D.P. Morrison,⁵ J.M. Moss,²⁷ F. Mühlbacher,⁴⁴ D. Mukhopadhyay,⁵¹ M. Muniruzzaman,⁶ J. Murata,^{38,39} S. Nagamiya,²⁰ J.L. Nagle,⁹ T. Nakamura,¹⁴ B.K. Nandi,⁶ M. Nara,⁴⁸ J. Newby,⁴⁶ P. Nilsson,²⁹ A.S. Nyanin,²³ J. Nystrand,²⁹ E. O'Brien,⁵ C.A. Ogilvie,¹⁶ H. Ohnishi,^{5,38} I.D. Ojha,^{49,93} K. Okada,³⁸ M. Ono,⁴⁸ V. Onuchin,¹⁵ A. Oskarsson,²⁹ I. Otterlund,²⁹ K. Oyama,⁸ K. Ozawa,⁸ D. Pal,⁵¹ A.P.T. Palounek,²⁷ V.S. Pantuev,⁴⁴ V. Papavassiliou,³⁴ J. Park,⁴² A. Parmar,³³ S.F. Pate,³⁴ T. Peitzmann,³⁰ J.-C. Peng,²⁷ V. Peresedov,¹⁷ C. Pinkenburg,⁵ R.P. Pisani,⁵ F. Plasil,³⁵ M.L. Purschke,⁵ A.K. Purwar,⁴⁴ J. Rak,¹⁶ I. Ravinovich,⁵¹ K.F. Read,^{35,46} M. Reuter,⁴⁴ K. Reygers,³⁰ V. Riabov,^{37,40} Y. Riabov,³⁷ G. Roche,²⁸ A. Romana,²⁵ M. Rosati,¹⁶ P. Rosnet,²⁸ S.S. Ryu,⁵² M.E. Sadler,¹ N. Saito,^{38,39} T. Sakaguchi,^{8,50} M. Sakai,³² S. Sakai,⁴⁸ V. Samsonov,³⁷ L. Sanfratello,³³ R. Santo,³⁰ H.D. Sato,^{24,38} S. Sato,^{5,48} S. Sawada,²⁰ Y. Schutz,⁴⁵ V. Semenov,¹⁵ R. Seto,⁶ M.R. Shaw,^{1,27} T.K. Shea,⁵ T.-A. Shibata,^{47,38} K. Shigaki,^{14,20} T. Shiina,²⁷ C.L. Silva,⁴¹ D. Silvermyr,^{27,29} K.S. Sim,²² C.P. Singh,³ V. Singh,³ M. Sivertz,⁵ A. Soldatov,¹⁵ R.A. Soltz,²⁶ W.E. Sondheim,²⁷ S.P. Sorensen,⁴⁶ I.V. Sourikova,⁵ F. Staley,¹⁰ P.W. Stankus,³⁵ E. Stenlund,²⁹ M. Stepanov,³⁴ A. Ster,²¹ S.P. Stoll,⁵ T. Sugitate,¹⁴ J.P. Sullivan,²⁷ E.M. Takagui,⁴¹ A. Taketani,^{38,39} M. Tamai,⁵⁰ K.H. Tanaka,²⁰ Y. Tanaka,³² K. Tanida,³⁸ M.J. Tannenbaum,⁵ P. Tarján,¹¹ J.D. Tepe,^{1,27} T.L. Thomas,³³ J. Tojo,^{24,38} H. Torii,^{24,38} R.S. Towell,¹ I. Tserruya,⁵¹ H. Tsuruoka,⁴⁸ S.K. Tuli,³ H. Tydesjö,²⁹ N. Tyurin,¹⁵ H.W. van Hecke,²⁷ J. Velkovska,^{5,44} M. Velkovsky,⁴⁴ L. Villatte,⁴⁶ A.A. Vinogradov,²³ M.A. Volkov,²³ E. Vznuzdaev,³⁷ X.R. Wang,¹³ Y. Watanabe,^{38,39} S.N. White,⁵ F.K. Wohn,¹⁶ C.L. Woody,⁵ W. Xie,⁶ Y. Yang,⁷ A. Yanovich,¹⁵ S. Yokkaichi,^{38,39} G.R. Young,³⁵ I.E. Yushmanov,²³ W.A. Zajc,^{9,†} C. Zhang,⁹ S. Zhou,⁷ S.J. Zhou,⁵¹ and L. Zolin¹⁷

(PHENIX Collaboration)

¹Abilene Christian University, Abilene, TX 79699, USA

²Institute of Physics, Academia Sinica, Taipei 11529, Taiwan

³Department of Physics, Banaras Hindu University, Varanasi 221005, India

⁴Bhabha Atomic Research Centre, Bombay 400 085, India

⁵Brookhaven National Laboratory, Upton, NY 11973-5000, USA

⁶University of California - Riverside, Riverside, CA 92521, USA

⁷China Institute of Atomic Energy (CIAE), Beijing, People's Republic of China

- ⁸Center for Nuclear Study, Graduate School of Science, University of Tokyo, 7-3-1 Hongo, Bunkyo, Tokyo 113-0033, Japan
⁹Columbia University, New York, NY 10027 and Nevis Laboratories, Irvington, NY 10533, USA
¹⁰Dapnia, CEA Saclay, F-91191, Gif-sur-Yvette, France
¹¹Debrecen University, H-4010 Debrecen, Egyetem tér 1, Hungary
¹²Florida State University, Tallahassee, FL 32306, USA
¹³Georgia State University, Atlanta, GA 30303, USA
¹⁴Hiroshima University, Kagamiyama, Higashi-Hiroshima 739-8526, Japan
¹⁵Institute for High Energy Physics (IHEP), Protvino, Russia
¹⁶Iowa State University, Ames, IA 50011, USA
¹⁷Joint Institute for Nuclear Research, 141980 Dubna, Moscow Region, Russia
¹⁸KAERI, Cyclotron Application Laboratory, Seoul, South Korea
¹⁹Kangnung National University, Kangnung 210-702, South Korea
²⁰KEK, High Energy Accelerator Research Organization, Tsukuba-shi, Ibaraki-ken 305-0801, Japan
²¹KFKI Research Institute for Particle and Nuclear Physics (RMKI), H-1525 Budapest 114, POBox 49, Hungary
²²Korea University, Seoul, 136-701, Korea
²³Russian Research Center “Kurchatov Institute”, Moscow, Russia
²⁴Kyoto University, Kyoto 606, Japan
²⁵Laboratoire Leprince-Ringuet, Ecole Polytechnique, CNRS-IN2P3, Route de Saclay, F-91128, Palaiseau, France
²⁶Lawrence Livermore National Laboratory, Livermore, CA 94550, USA
²⁷Los Alamos National Laboratory, Los Alamos, NM 87545, USA
²⁸LPC, Université Blaise Pascal, CNRS-IN2P3, Clermont-Fd, 63177 Aubiere Cedex, France
²⁹Department of Physics, Lund University, Box 118, SE-221 00 Lund, Sweden
³⁰Institut für Kernphysik, University of Muenster, D-48149 Muenster, Germany
³¹Myongji University, Yongin, Kyonggido 449-728, Korea
³²Nagasaki Institute of Applied Science, Nagasaki-shi, Nagasaki 851-0193, Japan
³³University of New Mexico, Albuquerque, NM 87131, USA
³⁴New Mexico State University, Las Cruces, NM 88003, USA
³⁵Oak Ridge National Laboratory, Oak Ridge, TN 37831, USA
³⁶IPN-Orsay, Université Paris Sud, CNRS-IN2P3, BP1, F-91406, Orsay, France
³⁷PNPI, Petersburg Nuclear Physics Institute, Gatchina, Russia
³⁸RIKEN (The Institute of Physical and Chemical Research), Wako, Saitama 351-0198, JAPAN
³⁹RIKEN BNL Research Center, Brookhaven National Laboratory, Upton, NY 11973-5000, USA
⁴⁰St. Petersburg State Technical University, St. Petersburg, Russia
⁴¹Universidade de São Paulo, Instituto de Física, Caixa Postal 66318, São Paulo CEP05315-970, Brazil
⁴²System Electronics Laboratory, Seoul National University, Seoul, South Korea
⁴³Chemistry Department, Stony Brook University, SUNY, Stony Brook, NY 11794-3400, USA
⁴⁴Department of Physics and Astronomy, Stony Brook University, SUNY, Stony Brook, NY 11794, USA
⁴⁵SUBATECH (Ecole des Mines de Nantes, CNRS-IN2P3, Université de Nantes) BP 20722 - 44307, Nantes, France
⁴⁶University of Tennessee, Knoxville, TN 37996, USA
⁴⁷Department of Physics, Tokyo Institute of Technology, Tokyo, 152-8551, Japan
⁴⁸Institute of Physics, University of Tsukuba, Tsukuba, Ibaraki 305, Japan
⁴⁹Vanderbilt University, Nashville, TN 37235, USA
⁵⁰Waseda University, Advanced Research Institute for Science and Engineering, 17 Kikui-cho, Shinjuku-ku, Tokyo 162-0044, Japan
⁵¹Weizmann Institute, Rehovot 76100, Israel
⁵²Yonsei University, IPAP, Seoul 120-749, Korea
- (Dated: March 30, 2022)

We present the results of ϕ meson production in the K^+K^- decay channel from Au+Au collisions at $\sqrt{s_{NN}} = 200$ GeV as measured at mid-rapidity by the PHENIX detector at RHIC. Precision resonance centroid and width values are extracted as a function of collision centrality. No significant variation from the PDG accepted values is observed, contrary to some model predictions. The ϕ transverse mass spectra are fitted with a linear exponential function for which the derived inverse slope parameter is seen to be constant as a function of centrality. However, when these data are fitted by a hydrodynamic model the result is that the centrality-dependent freeze-out temperature and the expansion velocity values are consistent with the values previously derived from fitting identified charged hadron data. As a function of transverse momentum the collisions scaled peripheral-to-central yield ratio R_{CP} for the ϕ is comparable to that of pions rather than that of protons. This result lends support to theoretical models which distinguish between baryons and mesons instead of particle mass for explaining the anomalous (anti)proton yield.

PACS numbers: 25.75.Dw

*Deceased

†PHENIX Spokesperson:zajc@nevis.columbia.edu

I. INTRODUCTION

Relativistic heavy-ion experiments have a goal of producing matter at extreme temperatures and energy densities such that conditions are favorable for the transition to a deconfined state of quarks and gluons, the Quark Gluon Plasma (QGP). Theoretical calculations predict that the temperatures and energy densities which can be reached at the Brookhaven National Laboratory's Relativistic Heavy Ion Collider (RHIC) will exceed those needed for the formation of the QGP [1, 2, 3].

The production and decay of the ϕ meson have long been recognized as an important probe for the state of matter produced in relativistic heavy ion (RHI) collisions [4, 5, 6, 7, 8, 9, 10, 11, 12, 13, 14, 15, 16, 17, 18, 19, 20, 21]. In pp collisions the creation of the ϕ is suppressed according to the Okubo-Zweig-Iizuka rule [22]. Hence, if there is an enhancement of the ϕ yield in RHI collisions relative to pp collisions, this could be evidence of non-conventional production mechanisms such as strange quark coalescence via the formation and subsequent hadronization of the QGP. The fact that the ϕ yield is undistorted by feed-down from higher mass resonances makes it an attractive probe in this respect.

The decay modes of the ϕ , specifically the dilepton channels (e^+e^- or $\mu^+\mu^-$) and the K^+K^- channel, will probe the final state differently should the decay take place in the presence of the QGP-mixed or the completely hadronized phase. The dileptons will have insignificant interactions with the medium, while the kaons can scatter until freeze-out. The lifetime of the ϕ in vacuum is large (≈ 45 fm/c) compared to say a 10 fm sized interaction region. However, several theoretical calculations [13, 21, 23] predict that the ϕ mass and width could be significantly modified in either the hot or the cold nuclear medium. These medium induced effects could be manifested through measured shifts in the mass centroid of the resonance or changes in the resonance width. Also predicted are changes in the relative branching ratio between kaon and lepton pairs, with respect to the Particle Data Group (PDG [24]).

The production mechanism of strangeness in heavy ion collisions can be investigated through the measurement of the particle yields. In this paper, we study system size dependence by analyzing centrality selected data. A comparison between different systems can be made by normalizing to the number of participant pairs. The expectation is that for production dominated by soft processes, the yields scale as the number of participants. We compare the centrality dependence of strange and non-strange particle yields in order to reveal the possible flavor dependence.

An additional important question is whether the ϕ mesons participate in radial flow together with the other hadrons, or if they freeze-out earlier, as might be true if

the small vacuum cross sections of the ϕ with hadrons persist in the fireball. Previous measurements have yielded contradictory results [25, 26]. One of the important advantages of RHIC experiments is the capability to examine the momentum spectrum as a function of centrality for a variety of hadrons which should yield important additional information on the radial flow issue. A spectral shape analysis including a simultaneous treatment of the ϕ and the more abundant hadrons (π, K, p) will be presented here.

At high p_T , hadrons are primarily produced from the fragmentation of hard-scattered partons. One of the most exciting results from RHIC was the discovery of hadron suppression in central Au+Au collisions [27, 28] where this suppression is absent in d+Au collisions [29]. Surprisingly, it was also discovered that proton and anti-proton production at intermediate p_T (1.5–4.5 GeV/c) scales with the number of binary nucleon-nucleon collisions (N_{coll}) as would be expected for hard-scattering in the absence of any nuclear modification [30]. In fact, the intermediate p_T anti-proton to pion ratios were found to exceed by a factor of 3 the values expected from parton fragmentation [30, 31]. These experimental results lead to the conclusion that protons and pions have different production mechanisms at intermediate p_T [30]. One possible explanation invokes parton recombination from the QGP [32, 33, 34, 35]. A measurement of the nuclear modification factor for the ϕ meson, which has a mass comparable to the proton but carries only two quarks, is crucial for understanding the hadron production at intermediate p_T . In this work we have measured the nuclear modification factor through the ratio R_{CP} of central to peripheral yields scaled by their respective N_{coll} value.

To put our results into perspective, we begin by describing the currently available ϕ data obtained in RHI collisions. The production of ϕ mesons has been studied systematically at ever increasing \sqrt{s} from the AGS to RHIC. The E802 collaboration made the first observation of the ϕ in fixed target central collisions of 14.6A GeV Si+Au ($\sqrt{s_{NN}} = 5.39$ GeV) via the K^+K^- channel [36]. They obtained a ratio $N_\phi/N_{K^-} = 11.6\%$, roughly consistent with the ratio obtained in pp data over a wide range of \sqrt{s} [37]. The analysis of the E802 rapidity distributions indicated that the ϕ production scaled with the product of the K^+ and K^- separate yields, and that there was either significant rescattering of the ϕ after production or the production itself came after rescattering of the colliding participants.

Also at the AGS the E917 experiment has reported another ϕ measurement with 11.7A GeV Au+Au ($\sqrt{s_{NN}} = 4.87$ GeV) in the rapidity range $1.2 < y < 1.6$ in five centrality bins [38]. The observed yield of the ϕ increased towards more central collisions with a distinctly faster than linear dependence on the number of participants. The yield increase of the ϕ in central collisions was stronger than that of the π since the N_ϕ/N_π ratio in-

creased in central collisions. However, the N_ϕ/N_{K^+} and N_ϕ/N_{K^-} ratios were constant as a function of centrality.

At the SPS the NA49 experiment has measured ϕ production in pp , p +Pb, and Pb+Pb collisions with $E_{\text{beam}}=158A$ GeV ($\sqrt{s_{NN}} = 17.5$ GeV) in the rapidity range $3.0 < y < 3.8$ [39]. Relative to the pp yields, these data showed that the ratio of the ϕ yield to the π yield in central Pb+Pb collisions was enhanced by a factor 3.0 ± 0.7 . Another SPS collaboration, NA38/NA50, has measured the ϕ in the $\mu^+\mu^-$ channel [40, 41], for which the extracted effective temperature and dN/dy differ from those obtained in the K^+K^- channel in the same systems. The yield difference between the two SPS experiments has been calculated to be factors of 2–4 [42], with the NA38/NA50 result being higher.

The first measurement of the ϕ meson at RHIC was reported by the STAR collaboration [43], in the collisions of Au+Au at $\sqrt{s_{NN}}=130$ GeV at three centralities, 0–11%, 11–26%, and 26–85% in the rapidity range $-0.5 < y < +0.5$. The extracted temperature T and the ratio N_ϕ/N_h did not vary with centrality.

One may summarize the current state of knowledge of ϕ production in heavy ion collisions by stating that the topic remains highly unexplored territory. The heavy-ion measurements do indicate that the observed ϕ yield is not a simple linear superposition of nucleon-nucleon collisions. Rather the data imply the influence of some collective effects. Whether those effects are induced by cold and/or hot nuclear matter, there do not yet exist definitive measurements. Moreover, there has not been so far precise enough heavy-ion data which can address the question of the change in the ϕ mass or its width in the cold nuclear or the hot QGP medium. And except for one experiment measuring the dimuon channel, there is a scarcity of useful quantitative information in heavy ion collisions concerning the ϕ decay into dileptons.

In this paper we report on a measurement of the ϕ yield at mid-rapidity in collisions of Au+Au beams from RHIC at $\sqrt{s_{NN}} = 200$ GeV as measured in the K^+K^- channel by the PHENIX detector. The paper is organized as follows. In Section II we give a short review of the PHENIX detector configuration. In Section III we describe the data analysis procedure. Section IV presents and discusses the results. The first precision measurements of ϕ mass and width values obtained in relativistic heavy ion collisions as a function of centrality are given in Section IV–A. Absolute yields as a function of p_T for three centrality bins are shown in Section IV–B. The centrality dependence of yields and ratios are studied in Section IV–D. In Section IV–D the spectra shapes are interpreted in the framework of a hydrodynamical model and the freeze-out conditions are extracted. Finally, the nuclear modification factor R_{CP} for the ϕ is obtained and compared to those of pions and protons in Section IV–E.

II. PHENIX DETECTOR

The PHENIX detector consists of two spectrometer arms at near zero rapidity, two forward rapidity muon spectrometers, and three global event characterization detectors. The central arm spectrometers, shown schematically in Fig. 1, are located East and West of the beam line with $\pi/2$ radian azimuthal coverage each. These spectrometers are designed to detect photons, electrons, and charged hadrons. The ϕ data for this paper were obtained with the central arm detector subsystems which provide high resolution particle identification and momentum reconstruction. A complete description of the PHENIX apparatus has been published elsewhere [44, 45, 46, 47, 48, 49]. We present a brief review of the relevant detector subsystems in the following sections.

A. Global Detectors

The global detectors furnish the start time signals, collision vertex measurements, and interaction centrality. The centrality for events in the Au+Au collisions is determined [50] by combining the data from two subsystems: the Zero Degree Calorimeters (ZDC) [48] and the Beam-Beam Counters (BBC) [47]. The ZDC are hadronic calorimeters located 18 m downstream and upstream of the interaction point along the beam line. These calorimeters detect the energy carried by spectator neutrons. The BBC are Čerenkov telescopes placed ± 1.44 m to the center of the beam collision region in the pseudo-rapidity region $3.0 < |\eta| < 3.9$. The correlation between the ZDC energy sum and the charge sum recorded in the BBC determines the centrality of the collision event. The BBC data also determine the longitudinal collision coordinate (z_{vertex}) and the start time for the time-of-flight measurements.

B. Central Arm Detectors

The central arm spectrometers [49] in PHENIX provide charged particle tracking and particle identification. This analysis was done with the East arm spectrometer. The $\phi \rightarrow K^+K^-$ decay kinematics are such that the PHENIX detector has negligible acceptance for the very low p_T ϕ particles which would decay into East-West kaon pairs. The data included information from the drift chamber (DC), the pad chambers (PC1 and PC3), the high resolution time-of-flight wall (TOF), and the electromagnetic calorimeter (EMCal) lead-scintillator detectors (PbSc), as depicted in Fig. 1.

Pattern recognition and tracking of the charged particles are accomplished using the DC information by a combinatorial Hough transform method [51]. The DC

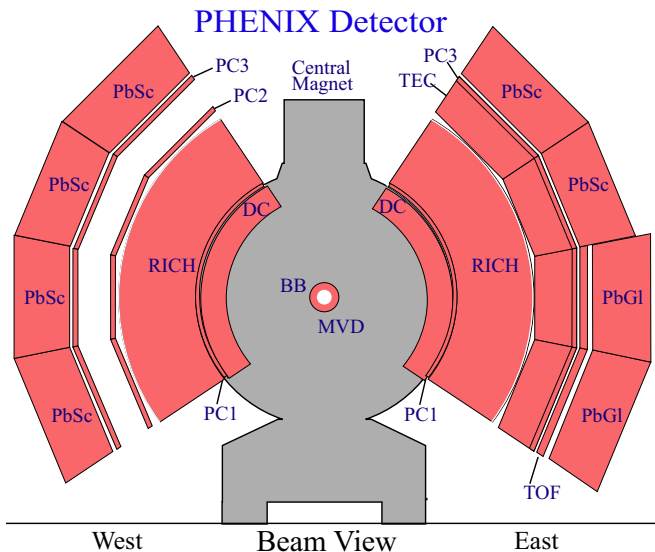


FIG. 1: Beam's eye view of the PHENIX central arm detector subsystems.

subsystem is located at an average radial distance of 2.2 m from the beam line. It is a projective tracking detector providing high precision measurements in the azimuthal XY plane, which are combined with the XYZ single spatial point measurement from the PC1 located at 2.45 m. These data, together with the BBC z_{vertex} information, are sufficient to determine the track's initial momentum vector whose magnitude is obtained with a resolution $\delta p/p \simeq 0.7\% \oplus 1.0\% \times p$ (GeV/c). The first term in this expression is due to the multiple scattering before the DC and the second term is the angular resolution of the DC. Based on identified mass measurements obtained with the TOF subsystem, the absolute momentum scale is known to $\pm 0.7\%$.

Tracks obtained from the DC/PC1 detectors are projected to the PC3, TOF, and PbSc detectors where associations can be made. The high resolution TOF subsystem provides one set of mass measurements while the PbSc detectors provide a geometrically independent set of mass measurements. The TOF wall is positioned 5.06 m from the beam line and consists of 960 scintillator slats oriented along the azimuthal direction. It is designed to cover $|\eta| < 0.35$ and $\Delta\phi = \pi/4$ in azimuthal angle.

The PbSc detector, covering half of the East arm and entire West arm, can also be used for hadron timing measurements. The present analysis uses the PbSc modules in the East Arm which are located at 5.1 m in radial distance from the beam line and cover a $\Delta\phi = \pi/4$ azimuthal range. This detector is constructed as separate towers of dimension $5.25 \times 5.25 \times 37$ cm³, in an alternating lead-scintillator sandwich type structure ("shish-kebob"), approximately 18 radiation lengths in depth. As illustrated in Fig. 1 the TOF and the PbSc sectors are completely non-overlapping.

TABLE I: Average number of participants and collisions in Au + Au reaction at RHIC for different centralities determined from a Glauber model[29]. The error associated with each number is the systematic error.

Centrality (%)	$\langle N_{\text{part}} \rangle$	$\langle N_{\text{coll}} \rangle$
0 - 10	325.2 ± 3.3	955.4 ± 93.6
10 - 20	234.6 ± 4.7	602.6 ± 59.3
20 - 40	140.4 ± 4.9	296.8 ± 31.1
10 - 40	171.8 ± 4.8	398.7 ± 40.5
40 - 60	59.9 ± 3.5	90.6 ± 11.8
60 - 92	14.5 ± 2.5	14.5 ± 4.0
40 - 92	32.0 ± 2.9	45.2 ± 7.3
Min. bias	109.1 ± 4.1	257.8 ± 25.4

III. DATA ANALYSIS

In this section, we describe the event and track selection, particle identification, the details of K^+K^- pair reconstruction, and the corrections for geometrical acceptance, particle decay in flight, multiple scattering, and detector occupancy factors, all of which couple into deriving the ϕ meson spectra.

A. Event Selection

The events selected for this analysis were based on the PHENIX minimum-bias trigger provided by the beam-beam counters (BBC) and zero-degree calorimeters (ZDC). As noted previously, the centrality of each Au + Au collision event was determined by correlating the BBC charge sum and the ZDC total energy [50]. The PHENIX minimum-bias data sample included $92.2^{+2.5}_{-3.0}\%$ of the 6.9 barn Au + Au total inelastic cross section [29]. This analysis used 20 million minimum-bias events with a vertex position within $|z_{\text{vertex}}| < 30$ cm.

To study the centrality dependent physics, we divided these events into different centrality bins. For the ϕ meson line shape analysis, we used five centrality bins: 0–10%, 10–20%, 20–40%, 40–60% and 60–92%. The transverse mass (m_T) spectra were reconstructed for three centrality bins: 0–10%, 10–40% and 40–92%. These bin divisions were chosen to have approximately equal statistical significance for their respective data points. The centrality of collisions is additionally characterized by the average number of participants ($\langle N_{\text{part}} \rangle$) and the average number of binary nucleon–nucleon collisions ($\langle N_{\text{coll}} \rangle$). These two global quantities, shown in Table I as a function of centrality, are derived from a Glauber model calculation [29].

B. Track Selection

Only tracks with valid information from the DC and the PC1 were used for the analysis. These tracks were then confirmed by matching the projected and associated hit information at the TOF wall for the TOF analysis, or at the PC3 and the EMCal for the PbSc analysis. The differences between the actual azimuthal and longitudinal hit coordinates compared to the projected hit coordinates were determined. These tracking coordinate residuals were converted to standard deviation residuals by a momentum dependent function which computed the expected residual coordinate value. On this basis, a 3σ track matching cut was used to accept track associations. Lastly, for the TOF wall, an energy loss cut is applied on the analog signal height from the scintillator slat. This cut has been described in a previous publication [50].

C. Particle Identification

As mentioned earlier, the PHENIX central arm spectrometer utilizes the high resolution TOF wall and PbSc modules for hadron mass identification. The kaons in the TOF wall were identified via reconstructed momentum combined with a time of flight measurement. The timing resolution of this subsystem is $\sigma \simeq 115$ ps. A momentum range of 0.3–2.0 GeV/c was selected in order to compute the mass distributions¹. Fig. 2 shows the mass-squared distribution of all tracks passing through the TOF module for six different momentum bins. The kaons were identified by applying a 2σ mass-squared cut, which is shown by the shaded region in each plot.

The particle identification with the electromagnetic calorimeter modules is sensitive to the fact that the electromagnetic and hadronic interactions produce quite different patterns of energy sharing between calorimeter towers [52]. As a consequence, the hadron timing properties of the PbSc depend on the energy deposited on the central tower of the cluster, particle momentum, particle type, charge, angle of incident of the track, *etc.* The PbSc hadronic timing response was corrected for these effects and we obtained an overall timing resolution of $\sigma \simeq 450$ ps which is sufficient to enable a clear π/K separation within $0.3 < p \text{ (GeV/c)} < 1.0$ using a 2σ mass-squared selection criterion. In Fig. 3 the mass-squared distributions are plotted for four different momentum slices for all tracks passing through PC3 and PbSc. The identified kaons are also shown in the figure

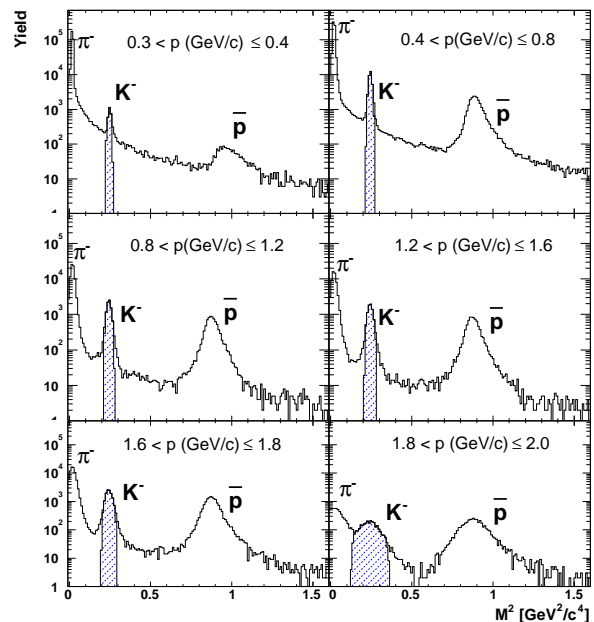


FIG. 2: Mass-squared distribution of all selected tracks passing through the TOF for six selected momentum bins. The identified kaons within 2σ mass-squared boundaries at the different momentum bins are shown by the shaded region on each plot.

by the 2σ width shaded histograms superimposed on the M^2 distributions for all tracks in different momentum bins.

D. K^+K^- Invariant Mass spectra and ϕ Signal Extraction

All identified K^+ and K^- tracks in a given event were combined to form the invariant pair mass distributions. Three different pair combinations were used. These are

- Both K^+ and K^- identified by the TOF detector (TOF–TOF combination),
- K^+ identified with TOF and K^- identified with PbSc (TOF–PbSc combination), and
- Both K^+ and K^- identified with PbSc detector (PbSc–PbSc combination).

We did not use the K^+ from PbSc and K^- from TOF in the b) combination. This is due to the fact that the PHENIX central arm geometry, in the presence of a 0.8 T-m magnetic field, does not have any acceptance for such pairs below an invariant mass of $1.06 \text{ GeV}/c^2$ in the TOF–PbSc combination.

A large combinatorial background is inherent to the K^+K^- pair invariant mass distribution. The combinatorial background was estimated by an event mixing method in which all K^+ tracks from one event were

¹ The mass-squared for each track is defined as, $M^2 = p^2(t^2c^2/L^2 - 1)$, where p is the momentum, t is the time of flight, c is the speed of light and L is the length of the path traversed by the track from vertex to the detector.

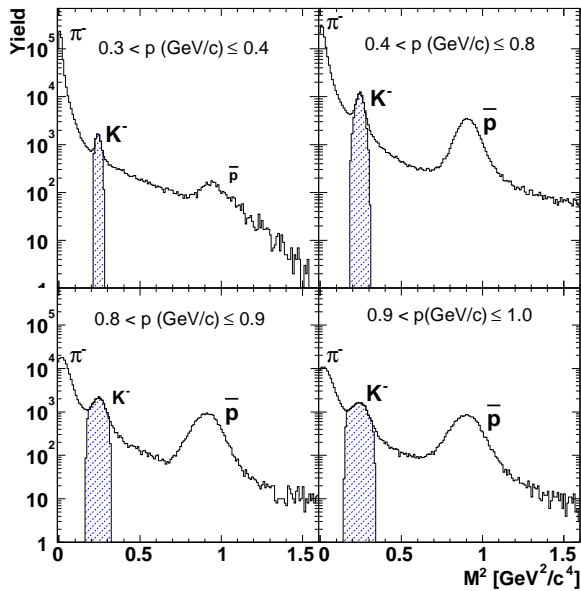


FIG. 3: Mass-squared distribution of all selected tracks passing through the PbSc for four momentum bins. The identified kaons within 2σ mass-squared boundaries at the different momentum bins are shown by the shaded region on each plot.

combined with K^- tracks of ten other events within the same centrality and vertex class. The mixed event technique reproduces the shape of the unlike sign combinatorial background. Finally, the size of the combinatorial background is obtained by normalizing the mixed event invariant mass spectra to $2\sqrt{N_{++}N_{--}}$ where N_{++} and N_{--} represent the measured yields in K^+K^+ and K^-K^- mass distributions respectively. This normalization is derived analytically starting from the assumption that the number of K^\pm tracks per event follows a Poisson distribution. A complete derivation of this is given in Appendix A.

The ability of this event mixing method to reproduce correctly the shape of the combinatorial background distribution was confirmed by constructing, in a similar way, the mixed-event like-sign spectrum and comparing it to the same-event like-sign pair distribution. The assumption is that the like-sign pair distributions are purely combinatoric. For the three detector combinations TOF-TOF, TOF-PbSc and PbSc-PbSc, the ratio of the measured and combinatorial like-sign invariant mass distributions were found to be consistent with 1.0 as a function of the pair mass within statistical errors for all centrality bins. As an example, in Fig. 4 we plot the measured and combinatorial “++” and “--” invariant mass distributions and their ratios for the TOF-PbSc combination as a function of the invariant mass of K^+K^+ and K^-K^- pairs for minimum-bias events. As can be seen from the figures, these ratios are equal to the expected value of 1.0 within the statistical fluctuations.

The systematic uncertainty associated with this normalization procedure was estimated to vary between 0.5–2% for the different centralities in the different detector combinations. When we added all data together to derive the ϕ spectrum, the range of the systematic uncertainty reduced to 0.7–1.0%.

Finally, the ϕ meson signal was obtained by subtracting the combinatorial background from the measured unlike-sign invariant mass spectrum. An example of the K^+K^- invariant mass spectrum for the TOF-PbSc combination is shown in Fig. 5 where we plotted the measured and scaled mixed event invariant mass distributions for minimum-bias events. The lower panel of the figure shows the subtracted mass spectrum. The corrected yield of the ϕ mesons from the experimental data is then determined by integrating the subtracted invariant mass spectrum within a mass window of ± 5 MeV/ c^2 about the measured ϕ mass centroid. This narrow mass window was used as it provided a better signal-to-background ratio compared with a wider window. Since we will show that there is no significant centrality dependence of the intrinsic width, then the extracted yields as a function of centrality are not being biased by the use of a constant integration window. The systematic effect of the mass integration window itself on the corrected yield was studied by varying the stated integration limit and found to contribute 2.6–3.2%, depending on centrality, to the total systematic uncertainty in the integrated yield.

E. Acceptance, Decay and Multiple Scattering Corrections

The ϕ meson yields were corrected for the geometrical acceptance of the detectors, in-flight kaon decay, multiple scattering effects, and nuclear interactions with materials in the detector using the PISA software package which is a GEANT-based [53] Monte Carlo detector simulation of the PHENIX detector. The simulation was carried out by generating 34 million single ϕ mesons in a ± 0.6 rapidity interval with an exponential transverse momentum distribution

$$dN/dp_T = p_T \exp(-m_T/(t_{fo} + \beta^2 M_\phi)) \quad (1)$$

with $t_{fo} = 157$ MeV and $\beta = 0.4$, *i.e.* an effective slope of $T = 320$ MeV in the range $0 < p_T < 10$ GeV/ c . The generated ϕ mesons were then propagated through the simulation package. In this simulation, the BBC, DC, PC, TOF and PbSc detector responses were tuned to match the real data by including their dead areas and by matching their track associations and mass-squared resolutions. That is, the track association and mass-squared cut boundaries in the Monte Carlo analysis were parameterized to match the real data. The K^+K^- pair acceptance efficiency as a function of transverse mass was calculated as

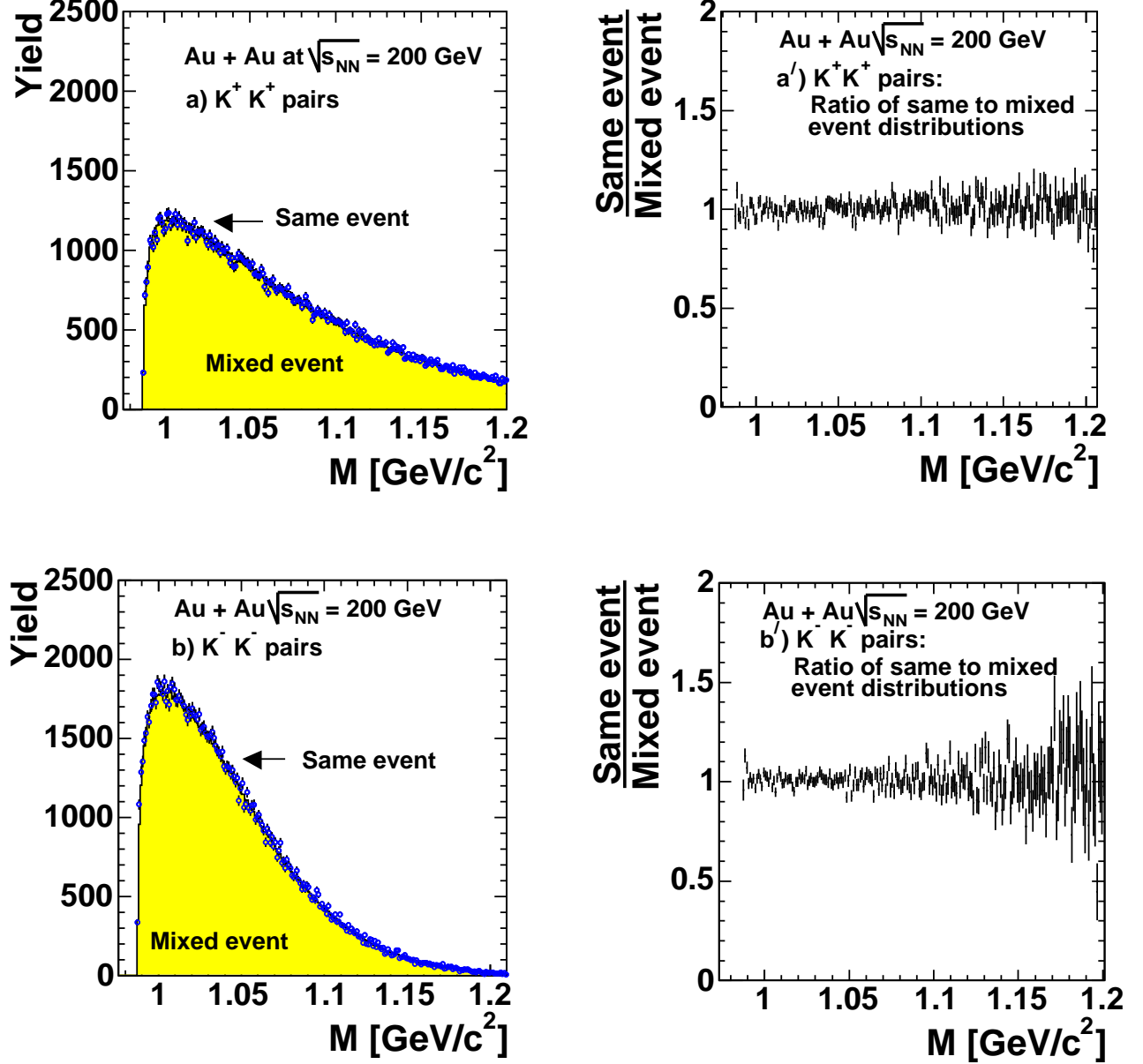


FIG. 4: K^+K^+ [(a) and (a')] and K^-K^- [(b) and (b')] invariant mass spectra and ratio of real to mixed event spectra, respectively, for the TOF-PbSc combination.

$$\epsilon(m_T) = \frac{N_{\phi}^{\text{reconstructed}}(m_T)}{N_{\phi}^{\text{generated}}(m_T)} \quad (2)$$

The calculated acceptance efficiencies for the TOF-TOF, TOF-PbSc and PbSc-PbSc combinations are shown in Fig. 6 as a function of m_T . The points in the figure are located at the center of the bins. In the actual m_T spectra, the proper bin centroids were used. The figure shows that the TOF detector (closed circles) has low acceptance for the low momentum kaon pairs due to their

large opening angles. On the other hand, the TOF covers the largest m_T range for the ϕ particles. As a result, the TOF efficiency function increases towards higher transverse mass. In contrast, the TOF-PbSc (open squares) and PbSc-PbSc (closed triangles) combinations offer better low pair momentum acceptance than the TOF. However, the high momentum kaon identification limit in the PbSc leads to the efficiency function decreasing at the highest transverse mass values. The systematic error associated with the acceptance correction factor originates from

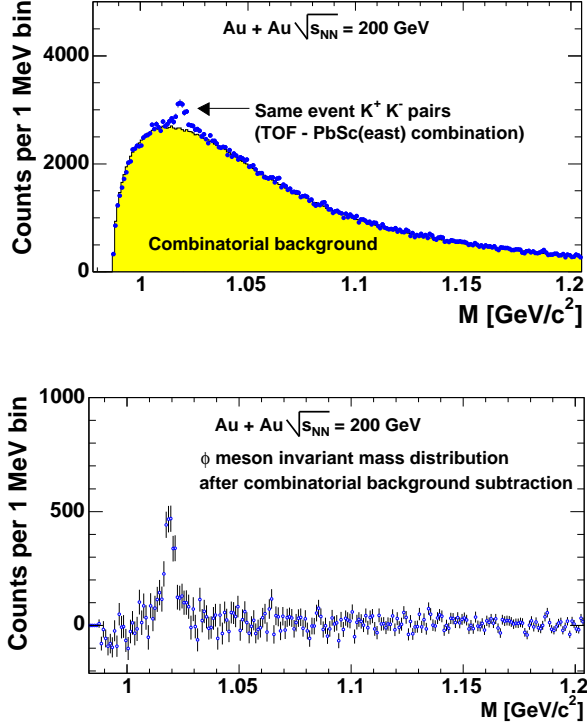


FIG. 5: K^+K^- invariant mass spectra for the measured and mixed events (top half) in the TOF-PbSc combination, and the subtracted mass spectrum showing the ϕ meson peak clearly above the background (bottom half).

- i) tuning of detector alignments and mass-squared parameters in the Monte Carlo with reference to the real data ($\sim 3\%$), and
- ii) systematics in the fiducial geometries in the data and the Monte Carlo ($\sim 12\%$).

F. Detector Occupancy Correction

The high multiplicity environment in the heavy ion collisions produces multiple hits in a detector cell such as in the slats of the TOF or in the towers of the PbSc. These occupancy effects reduce the track reconstruction efficiency in central collisions compared to that in peripheral collisions, and these occupancy dependent effects need to be accounted for in calculating the invariant yields. The multiplicity dependent efficiency ($\epsilon_{\text{occupancy}}$) factors were calculated by embedding simulated K^+K^- pairs into real data events. This study was done for different centrality bins from 0 to 92% in steps of 10%. We calculated the multiplicity dependent efficiencies for TOF-TOF, TOF-PbSc and PbSc-PbSc pairs separately. The systematic uncertainty associated with the embedding procedure was estimated for the three centrality bins

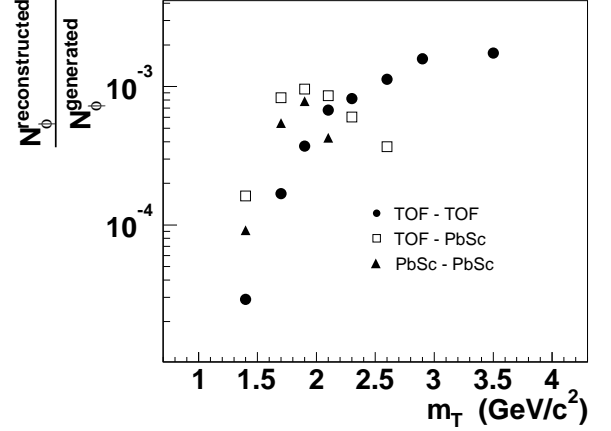


FIG. 6: Detector acceptance efficiency vs transverse mass of the simulated K^+K^- pairs for the TOF-TOF, TOF-PbSc and PbSc-PbSc combinations. The statistical errors are smaller than the size of the data symbols.

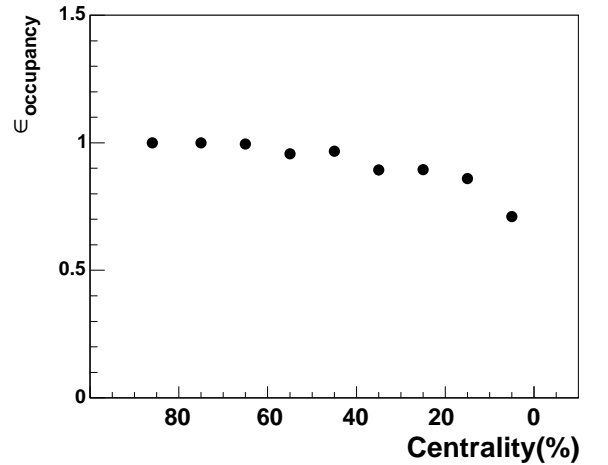


FIG. 7: Multiplicity (occupancy) dependent efficiency correction for detecting the ϕ meson in the PHENIX detector as a function of the collision centrality. The most central collisions are to the right, the most peripheral collisions are to the left. The statistical errors are less than the size of the data points.

used in the yield determinations, namely 0 - 10%, 10 - 40% and 40 - 92%. The systematic errors, calculated by estimating the occupancy efficiency corrections for different track confirming criteria, were found to vary from 7% to 10% for the three centrality bins used here, independent of the pair momenta. Fig. 7 shows the $\epsilon_{\text{Occupancy}}$ factors as a function of collision centrality for the K^+K^- pairs both identified in the TOF detector. The occupancy dependent efficiency factors were found to be independent of the transverse momenta of the pairs.

IV. RESULTS AND DISCUSSION

In this section, we present and discuss the results of our measurements, which consist of: 1) the ϕ line shape analysis, 2) the transverse mass spectra analysis, 3) the integrated yields and ratios analysis, 4) hydrodynamical fits to π^\pm , K^\pm , p , \bar{p} and ϕ transverse momentum spectra, and 5) the centrality dependence of the yields and nuclear modification factor R_{CP} as compared to that of pions and (anti)protons.

A. Line Shape Analysis

The invariant mass spectra of the ϕ mesons are obtained by subtracting the combinatorial backgrounds from the same event K^+K^- mass spectra. The details of the combinatorial background analysis were described in section III D. For the best statistical precision, we combine data from TOF and PbSc detectors to analyze the ϕ mass centroids and widths at the five different centrality bins.

Fig. 8 shows the minimum-bias $\phi \rightarrow K^+K^-$ invariant mass spectrum for the PHENIX data. The subtracted ϕ mass spectrum (lower panel), containing approximately 5100 ϕ in the fit region, is fitted with a relativistic Breit-Wigner (RBW) mass distribution function [38] convolved with a Gaussian experimental mass resolution function. Using Monte Carlo studies based on the experimentally measured single kaon momentum resolution, the experimental ϕ mass resolution is calculated to be $1.0 \text{ MeV}/c^2$. This pair mass resolution value is found to be almost constant across the kinematic region of acceptance.

The errors on the data points in Fig. 8 reflect the statistical errors only. The systematic errors associated with the mass centroid and width measurements originate from the magnetic field uncertainties in the kaon momentum determination and the combinatorial background normalization procedure. The minimum-bias line shape parameters (centroid and width) derived in our analysis are listed in Table II. The fitted minimum bias ϕ mass centroid and width are consistent at the one standard deviation (1σ) level with the PDG values², taking into account both systematic and statistical errors.

We investigated the centrality dependence of the ϕ meson line shapes. For each centrality bin, we again fitted the ϕ mass spectrum with the RBW function convolved with a Gaussian experimental ϕ mass resolution. The results are presented in Fig. 9. The left panel of the figure shows the centrality dependence of the fitted centroids.

² The PDG value for the ϕ mass centroid is $1019.456 \pm 0.020 \text{ MeV}/c^2$, and for the ϕ width the value is $4.26 \pm 0.05 \text{ MeV}/c^2$ [24].

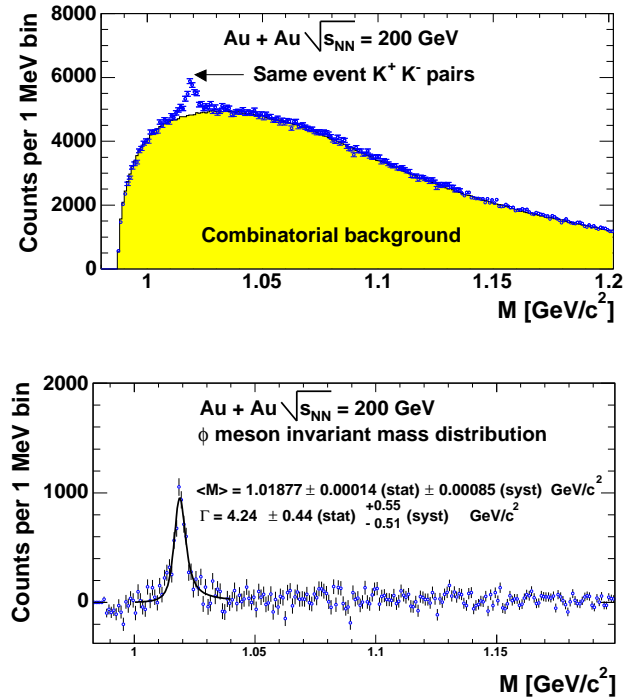


FIG. 8: Minimum-bias $\phi \rightarrow K^+K^-$ invariant mass spectrum using the kaons identified in the PHENIX detector. The top panel shows the same event (circles) and combinatorial background K^+K^- mass distributions. The bottom panel shows the subtracted mass spectrum fitted with Relativistic Breit-Wigner function convolved with the Gaussian resolution function.

TABLE II: ϕ meson mass centroid and width for the minimum-bias Au + Au collisions at $\sqrt{s_{NN}} = 200 \text{ GeV}$. The corresponding PDG values are $M_\phi = 1.019456 \text{ GeV}/c^2$, $\Gamma_\phi = 4.26 \text{ MeV}/c^2$

Parameter	Value
Centroid (GeV/c^2)	$1.01877 \pm 0.00014 \text{ (stat)} \pm 0.00085 \text{ (syst.)}$
Width (MeV/c^2)	$4.24 \pm 0.45 \text{ (stat)} \pm {}^{0.55}_{-0.51} \text{ (syst)}$

The upper and lower 1σ systematic error limits are indicated. The dotted line shows the PDG mass centroid. The solid line indicates the result obtained with a one-parameter constant fit through the measured data points. These results lead to two immediate conclusions. First, to within less than $1 \text{ MeV}/c^2$ there is no observed centrality dependence of the ϕ meson mass centroid, and second, the fitted centroids at all centralities are consistent with the PDG value within the statistical and systematic uncertainties of our measurements.

The ϕ mass widths, as shown in the right panel of the figure, are studied as a function of the centrality. The

error bar on each point shows the statistical error while the bands on the points indicate the systematic errors. The dotted line shows the PDG ϕ mass width. The solid line shows the results of the constant fit assumption to the data points. Again, within the random and systematic error limits shown, there is no convincing evidence of a variation of the ϕ width as a function of centrality.

The topic of medium effects on meson masses has been actively investigated in the recent literature [7, 8, 9, 10, 20, 23, 54, 55, 56]. The predictions are that for both cold and hot nuclear matter there could be a decrease of the ϕ mass value by a few MeV/ c^2 or even tens of MeV/ c^2 . Even more dramatically the width could increase by several multiples above the PDG value of 4.26 MeV/ c^2 . A sample of such predictions is given in Table III. However, one of the models [20] considers the $\phi \rightarrow K^+K^-$ channel largely insensitive to medium effects since the kaons are “unlikely to escape without reacting further, thus destroying any useful information possessed about the ϕ ”. In this sense the $\phi \rightarrow K^+K^-$ is inherently biased in that only ϕ decays which are unaffected by the medium changes, for example those produced peripherally, can be detected.

It is sometimes thought that since the vacuum $c\tau$ of the ϕ is ≈ 45 fm/ c there will be only limited sensitivity to medium effects in any case. However, if the resonance width were to actually increase by several times, as indicated in Table III, then the $c\tau$ would then approach or be even substantially less than 10 fm/ c , which is a size compatible with the expected collision volume. The dramatic width changes predicted in either cold or hot nuclear matter might be visible, at least in the dilepton channel if not also the K^+K^- channel, as a function of centrality.

The present mass centroid and width data, which are integrated over the available m_T range, rule out any major changes with respect to the PDG values. Specifically, the one parameter fit result of 3.97 ± 0.34 MeV/ c^2 obtained here excludes at the 99% confidence level a width value of 4.75 MeV/ c^2 or greater. Possibly at the lowest m_T values where the ϕ would remain longer in the collision volume, or with the availability of more finely binned centralities, there could be visible evidence of in medium effects. However, the current data sample is insufficient to explore these possibilities.

It seems clear from the current set of the theoretical models that an observed change in the ϕ width would not be itself indicative of a QGP formation. One would first have to constrain the cold nuclear medium effects on the ϕ as could be obtained in d+Au collisions, or by comparing peripheral Au+Au collision data results with central collision data. It is also important to measure the ϕ mass in the dilepton e^+e^- channel. That channel should be more sensitive to the ϕ which are produced deeper or earlier in the collision volume.

B. Spectral Shapes Analysis

At low m_T , the spectral shapes carry information about the kinetic freeze-out conditions. Since the centrality dependence reveals the effect of the system size on the fireball evolution it becomes desirable to study the centrality dependence of the spectral shapes. Transverse mass spectra were obtained in three centrality bins corresponding to 0–10%, 10–40% and 40–92% of the total geometrical cross-section. We count the same event K^+K^- pairs within a defined mass window (± 5 MeV/ c^2 with respect to the ϕ mass centroid) and estimate the number of combinatorial background pairs within that window. In each centrality bin, the data are divided into different m_T bins. The invariant mass spectrum for the same events and the background distributions are obtained for each of these m_T bins. Finally, the background is subtracted from the same event invariant mass spectrum within the aforementioned ± 5 MeV/ c^2 ϕ mass window to determine the number of reconstructed ϕ mesons within that m_T bin. The reconstruction of the ϕ in the Monte Carlo simulation takes into account the effect of the ϕ mass window size.

The ϕ mesons are reconstructed using kaons identified in the TOF and the PbSc detectors. Three detector combinations: TOF–TOF, TOF–PbSc, and PbSc–PbSc are used to obtain three independent transverse mass spectra. Fig. 10 shows the minimum-bias m_T spectra for the above three combinations. The combined result, which is the sum of the three combinations is also included. For better visibility of the data points, TOF–TOF, TOF–PbSc and PbSc–PbSc spectra are scaled by a factor of 0.5, 0.1 and 0.05, respectively. The m_T spectrum obtained from the PHENIX detector is fitted with the exponential function:

$$\frac{1}{2\pi m_T} \frac{d^2 N}{dm_T dy} = \frac{dN/dy}{2\pi T(T + M_\phi)} e^{-(m_T - m_\phi)/T} \quad (3)$$

where dN/dy and the inverse slope T are returned as two fitting parameters. The lines drawn through the TOF–TOF, TOF–PbSc and PbSc–PbSc spectra represent the same fit, but scaled with the same scaling factors as the data points. Comparison of the individual spectra to the fit obtained from the combined spectrum demonstrates the consistency between the different measurements, which have different systematic uncertainties. The TOF–TOF, TOF–PbSc and PbSc–PbSc spectra are also independently fitted using Eq. (3). The resulting dN/dy and T are tabulated in Table IV. Both statistical and systematic errors are quoted. The systematic errors on dN/dy originate from the systematic uncertainties associated with extraction of the yields in each m_T bin (see Appendix C) and the uncertainties from the fitting procedure. The latter is sensitive to the extrapolation of the m_T spectra to $m_T = m_\phi$. A detailed account of systematic errors on dN/dy and T in the full dataset from all sources is shown in Appendix C. We also fitted the TOF–

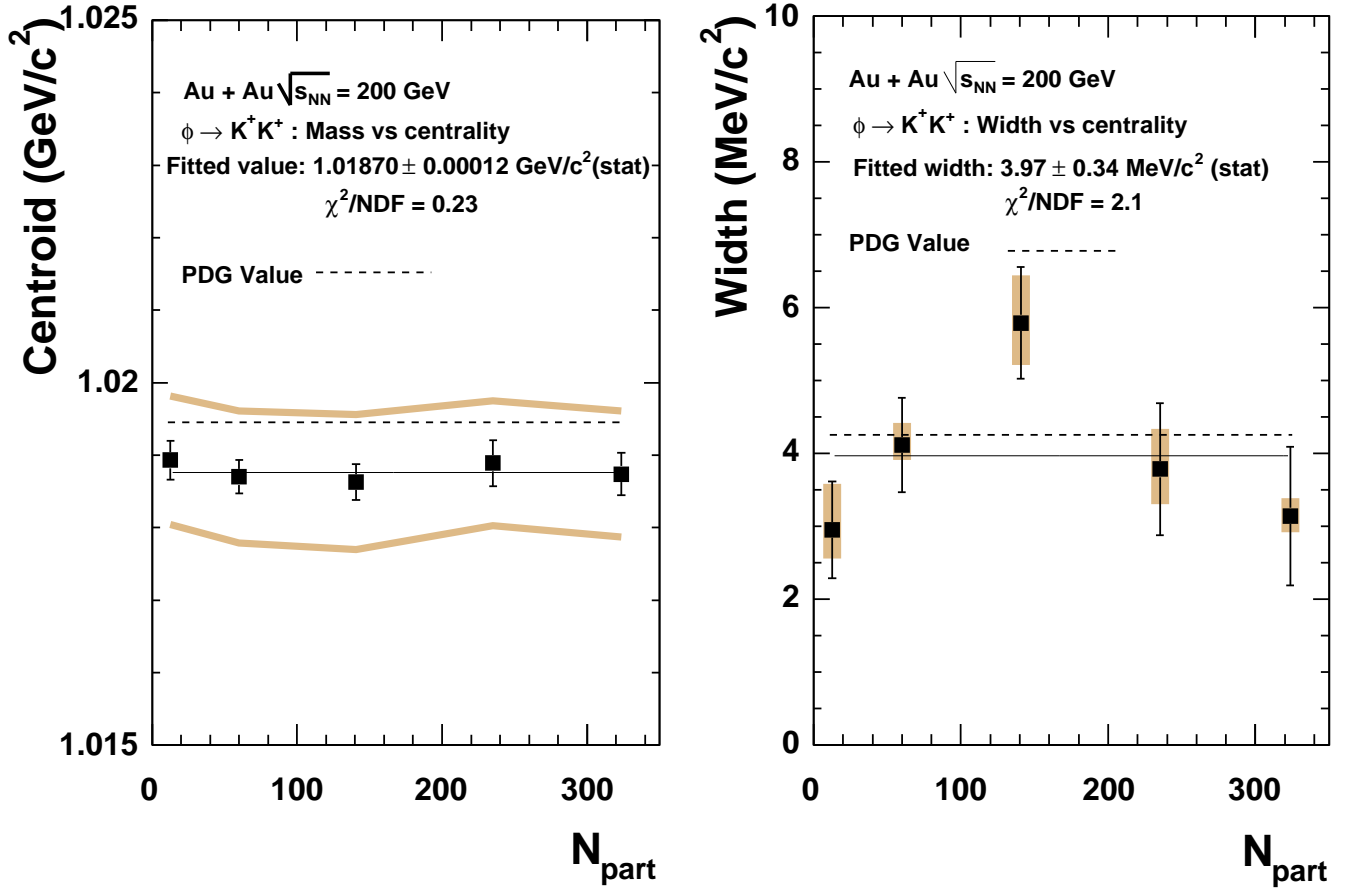


FIG. 9: Centrality dependence of the ϕ mass centroid (left) and ϕ intrinsic width (right), where the N_{part} to Centrality correspondence is given in Table I. For the mass centroid plot, the 1σ systematic error limits on the data points are shown by the two continuous bands. The dotted line shows the PDG centroid value ($1.019456 \text{ GeV}/c^2$). The solid line indicates the centroid value obtained from a one parameter fit assumption. For the width plot the systematic errors on the RBW widths are indicated as bands on each data point. Similarly the dotted line shows the PDG width value ($4.26 \text{ MeV}/c^2$), and the solid line shows a one parameter fit result for the measured data points.

TOF and TOF-PbSc data over the smaller m_T range of the PbSc-PbSc data and obtained consistent sets of dN/dy and T values from that check.

Fig. 10 and Table IV indicate that the three different analyses with different systematic uncertainties give consistent results. This allowed us to combine the results and make use of the maximum available statistics in each m_T bin. This combined spectrum was used to obtain the physics results discussed in the next sections.

Fig. 11 shows m_T spectra of the ϕ mesons in 0–10%, 10–40%, 40–92% and minimum bias centrality classes. The data points representing the invariant yield as a function of transverse momentum are given in Appendix B. Each spectrum is fitted with an m_T -exponential function Eq. (3). The ϕ yield per unit of rapidity (dN/dy) and inverse-slope (T) obtained from the fits are shown in

Table V, and summarized in Fig. 12 and Fig. 13³.

C. Yields and ratios

Hadron yields and ratios carry information about the chemical properties of the system. The yields of strange

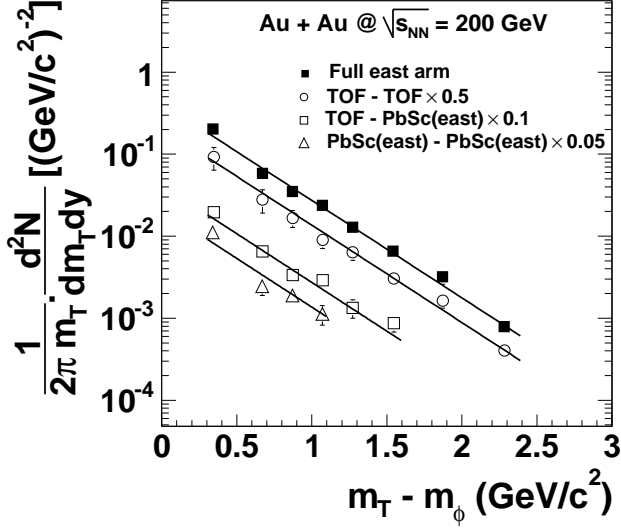
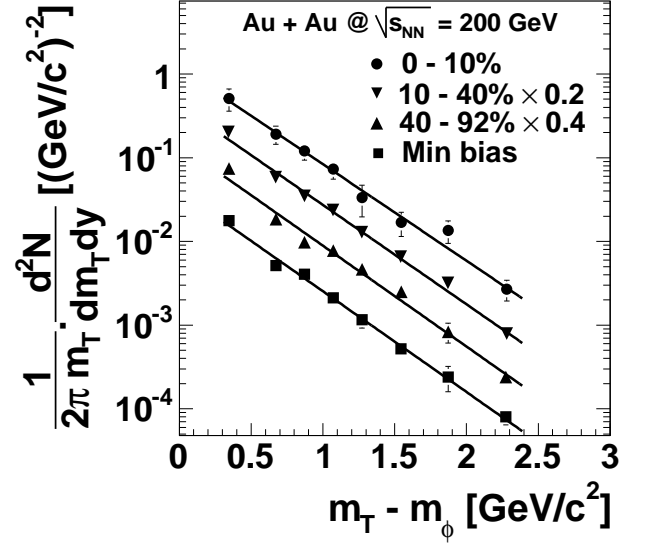
³ The STAR experiment at RHIC has recently reported its analysis of the $\phi \rightarrow K^+K^-$ data for Au+Au at $\sqrt{s_{NN}} = 200$ GeV[66]. The analyses for PHENIX and STAR have one common centrality bin, 0–10%, for which the extracted dN/dy are not in agreement. The STAR value is $6.65 \pm 0.35(\text{stat}) \pm 0.73(\text{sys})$, compared with the PHENIX value $3.94 \pm 0.60(\text{stat}) \pm 0.62(\text{sys})$. The discrepancy persists even if one eliminates the four lowest m_T data points from the STAR data set in order to fit over the same m_T range for both the STAR and the PHENIX data. There is not a discrepancy between the quoted inverse slope parameters.

TABLE III: Theoretical Predictions for Changes in the ϕ Resonance

Authors	Models	Environment	Predictions
Caberara and Vacas [23]	Chiral SU(3)	Cold hadronic	$M_\phi \rightarrow 1.011 \text{ GeV}$ $\Gamma_\phi \rightarrow 30 \text{ MeV}/c^2$
Pal, Ko, and Lin [13]	AMPT Chiral Lagrangian	Hot hadronic	$M_\phi \rightarrow 0.95 \text{ GeV}/c^2$ at twice normal nuclear density (ρ_0) $\Gamma_\phi \rightarrow 45 \text{ MeV}/c^2$ at $2\rho_0$ Suppression of $\phi \rightarrow K^+K^-$ relative to $\phi \rightarrow e^+e^-$
Oset and Ramos [21]	Kaon mass renormalization	Cold hadronic	M_ϕ unchanged $\Gamma_\phi \rightarrow 22 \text{ MeV}/c^2$
Smith and Haglin [20]	One boson exchange	Hot hadronic	M_ϕ unchanged $\Gamma_\phi \rightarrow 14\text{--}24 \text{ MeV}/c^2$
Blaizot and Galain [12]	Nambu-Jona-Lasino	Hot hadronic	$M_\phi \rightarrow 2M_K$ at $T \approx T_{\text{critical}}$ Γ_ϕ reduced by a factor of 6 $\phi \rightarrow K^+K^-$ disappears
Bi and Rafelski [14]	Bag Model Chiral Invariance	Hot hadronic	$M_\phi \rightarrow 1.029 \text{ GeV}/c^2$ at $T \approx T_{\text{critical}}$ $\Gamma_\phi \rightarrow 10 \text{ MeV}/c^2$

TABLE IV: Minimum-bias dN/dy and T for different subsystem combinations. The statistical and systematic errors are shown after the first and second \pm signs, respectively.

Subsystem combination	TOF-TOF	TOF-PbSc	PbSc-PbSc	Full Data Set
dN/dy	$1.16 \pm 0.17 \pm 0.19$	$1.37 \pm 0.15 \pm 0.22$	$1.47 \pm 0.26 \pm 0.27$	$1.34 \pm 0.09 \pm 0.21$
$T(\text{MeV})$	$380 \pm 18 \pm 22$	$385 \pm 34 \pm 28$	$311 \pm 47 \pm 65$	$366 \pm 11 \pm 18$

FIG. 10: Minimum-bias m_T spectra of the measured ϕ mesons for three different PHENIX subsystem combinations, with scale factors as indicated. The combined spectrum is fitted with an exponential function in m_T , Eq. (3). The lines drawn through the individual spectra (TOF-TOF, TOF-PbSc and PbSc-PbSc) represent the same fit parameters as in the minimum-bias case. Statistical error bars are shown.FIG. 11: m_T spectra of ϕ mesons for 0–10%, 10–40%, 40–92% and minimum-bias (0–92%) centrality classes, with scale factors as indicated. Each spectrum is fitted with an exponential function in m_T , Eq. (3), with the fit parameters listed in Table V. Statistical error bars are shown.

particles have been of particular interest as they help in understanding the strangeness enhancement in heavy ion collisions and the equilibration of strangeness. It is important to study these phenomena as a function of system

size. Centrality selected data can be particularly useful in this respect. Here we present the yield of the ϕ mesons at mid-rapidity as a function of centrality and compare this yield to the yields of other hadrons and the results

TABLE V: dN/dy and T for different centrality bins.

Centrality (%)	dN/dy	T (MeV)
0 – 10%	3.94 ± 0.60 (stat) ± 0.62 (syst)	376 ± 24 (stat) ± 20 (syst)
10 – 40%	2.22 ± 0.18 (stat) ± 0.35 (syst)	360 ± 13 (stat) ± 23 (syst)
40 – 92%	0.32 ± 0.03 (stat) ± 0.05 (syst)	359 ± 15 (stat) ± 16 (syst)
Minimum Bias	1.34 ± 0.09 (stat) ± 0.21 (syst)	366 ± 11 (stat) ± 18 (syst)

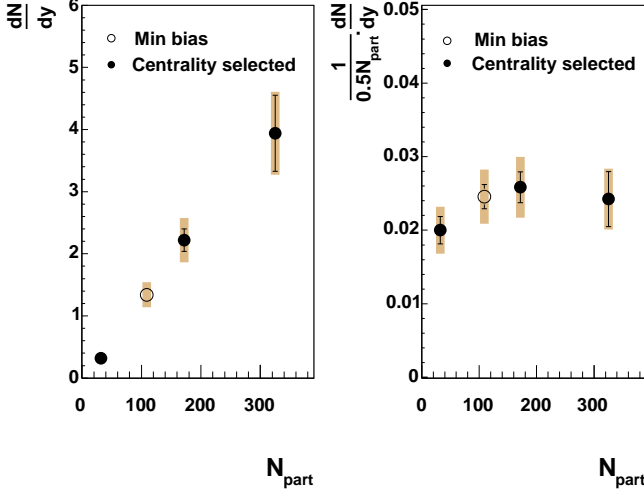


FIG. 12: Centrality dependence of ϕ yield at mid-rapidity. The value of dN/dy increases steadily with the number of participants (N_{part}) (left) whereas the dN/dy per participant pairs increases slightly from peripheral to mid-central events and saturates after that (right). The error bars indicate the statistical errors. The shaded boxes on each data point are the systematic errors.

from lower energy heavy ion collisions. The dN/dy of ϕ (shown in Fig. 12) is found to increase steadily with centrality. In the right panel, the yield is normalized to the number of participant pairs to take into account the size of the system. Within the error bars this normalized rapidity density is approximately independent of centrality with a possible slight increase from peripheral to the mid-peripheral collisions. The trend is quite different from lower energy results measured at the AGS. In [38], the yield of ϕ was reported to be increasing faster than linearly with the number of participants.

We now consider the ratio of strange to non-strange particles in order to understand the extent and mechanism of the strangeness enhancement in heavy ion collisions. The ratios K^+/π^+ and K^-/π^- , are shown in Fig. 14 (a)–(b). Both ratios show an increase of $\approx 60\%$ from peripheral to central collisions. Most of this increase is for $N_{part} < 100$. Only a mild increase or saturation is

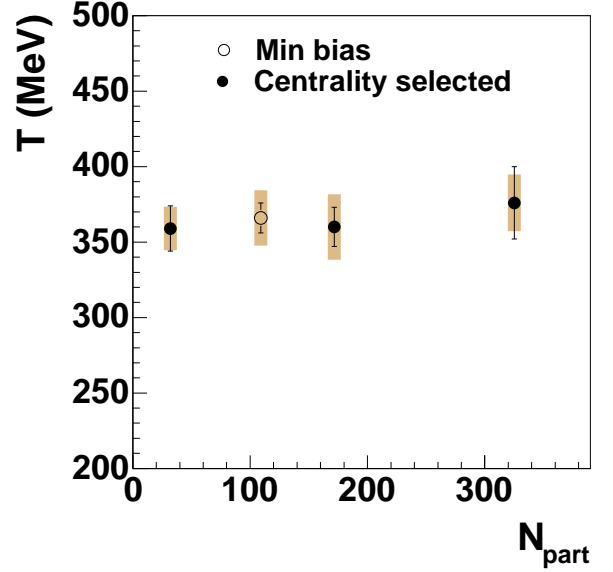


FIG. 13: Centrality dependence of the inverse slope, T .

observed from mid-central to the top centrality bin [50]. Fig. 14 (c)–(d) shows the centrality dependence of the ϕ/π and ϕ/K ratios. The limited statistics prevent us from extending the ϕ measurements into larger number of centrality bins spanning the more peripheral events. The ϕ/K ratio, in this limited number of centrality bins, is approximately flat as a function of centrality. The possibility of structure in the ϕ/π ratio is difficult to infer from our data within the error bars. One might expect to see some centrality dependence in the ϕ/π ratio because there is obviously a centrality dependence to the K/π ratio. However, we do not have enough centrality bins, nor enough signal in each bin, from which to conclusively identify a centrality dependence in ϕ/π . The flat behavior of the ϕ/K ratio indicates that there is no pronounced difference in the production of open (kaon) and hidden (ϕ) strangeness in heavy ion collisions at RHIC energies. Production in the hadronic stage via kaon coalescence $K^+K^- \rightarrow \phi$, seems to be excluded by that data, as it would result in an increase in ϕ/K^- as a function of N_{part} , which is not observed.

The collision energy dependence of the ϕ yield is shown in Fig. 15 where we plot the dN/dy per participant pair as a function of the number of participants for different

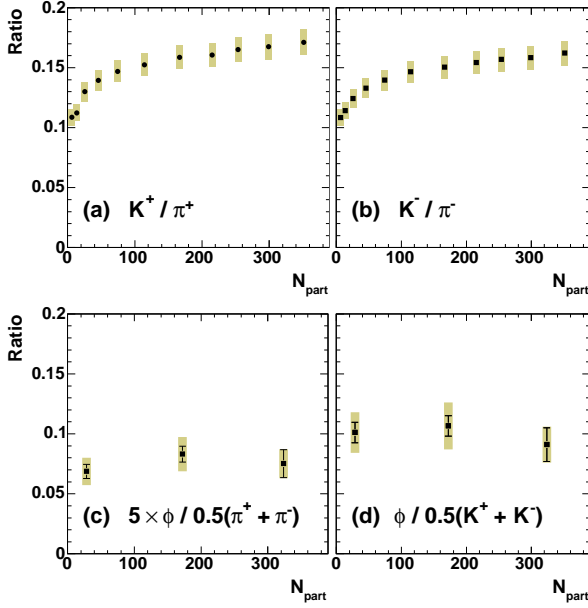


FIG. 14: Centrality dependence of particle ratios for (a) K^+/π^+ , (b) K^-/π^- , (c) $\phi/0.5(\pi^+ + \pi^-)$ (scaled by a factor of 5), (d) $\phi/0.5(K^+ + K^-)$ in Au+Au collisions at $\sqrt{s_{NN}} = 200$ GeV.

colliding energies. The figure indicates two aspects of ϕ meson production at various energies. First, as we go from AGS to SPS to RHIC, the ϕ meson yield per participant increases by an order of magnitude overall. Secondly, at the AGS energy, we find a steady increase of ϕ production per participant pair from peripheral to central collisions. It is worth mentioning that the NA50 experiment [25] at CERN SPS reported an increase in fiducial ϕ yield (in $\mu^+ \mu^-$ decay channel) per participant from peripheral to central collisions although the yield per participant showed saturation within error for the top centrality bins. The yield of ϕ mesons at RHIC, on the contrary, is found to be almost independent of centrality.

To investigate further the mechanism of ϕ enhancement with increase in collision energy, we study the two ratios ϕ/π and ϕ/K^- as a function of collision energy as illustrated in Fig. 16. The ϕ/π ratio is found to increase with the collision energy from AGS to RHIC. The ϕ/K^- ratio, on the other hand, remains almost constant within error bar with increasing collision energy.

D. Hydrodynamical Model Fits to the Spectral Shape Data

From the ϕ spectral data shown in the preceding sections, we can conclude that the transverse mass distributions are well described by an exponential distribution and are quite similar for all the centralities. There is little, if any, centrality dependence of the inverse slope parameter in the measured centrality bins, as shown in

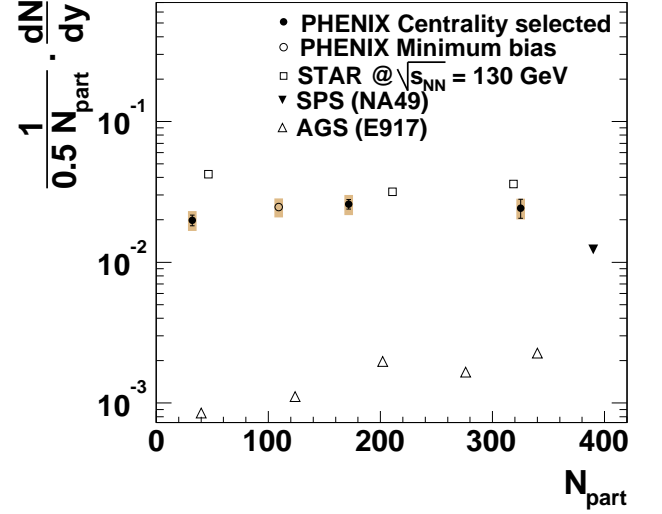


FIG. 15: Centrality dependence of ϕ yields at different collision energies. STAR data are from [43], NA49 data are from [39], and E917 are from [38].

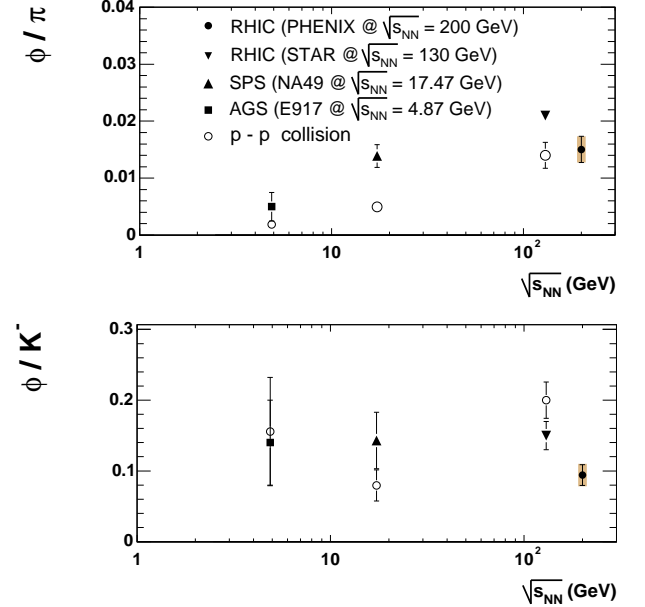


FIG. 16: ϕ/π (top half) and ϕ/K^- (bottom half) ratios as a function of collision energy. The data symbols have the same meanings in both the top and the bottom halves of the figure.

Fig. 13. The exponential behavior is expected for particle production from a thermal source.

If the system develops collective motion, particles experience a velocity boost resulting in an additional transverse kinetic energy component. This motivates the use of the transverse kinetic energy, *i.e.* transverse mass minus the particle rest mass, for studying flow effects. Traditionally, the CERN experiments [57, 58] have used simple exponential fits to the transverse kinetic energy dis-

tributions and often quote just one number, the inverse slope T , to characterize the spectra. These fits are usually done in the range $(m_T - m_0) < 1 \text{ GeV}/c^2$ in order to minimize the contribution from hard processes.

The results of such fits, obtained from previously published PHENIX π^\pm , K^\pm , p and \bar{p} data [50] are shown in Fig. 17. The slope parameters show a clear mass dependence, as expected from radial flow. The mass dependence increases from peripheral to central collisions indicating stronger collectivity in the more central events. The ϕ meson has mass similar to that of the proton. Hence we expect that if the ϕ participates in the collective flow then its inverse slope will be affected by this motion. For protons, the slope parameter changes significantly from peripheral to central collisions. As just noted, the ϕ inverse slopes shows no such centrality dependence. An important difference between the results obtained for p , \bar{p} and ϕ is that the former have been fitted within a limited low- m_T range ($(m_T - m_0) < 1 \text{ GeV}/c^2$) as motivated above. In the case of the ϕ the full measured range has been used for the fit due to having limited data at low- m_T . As shown in Fig. 11, the three data points below $1 \text{ GeV}/c^2$ are consistent with the fit over the entire m_T range.

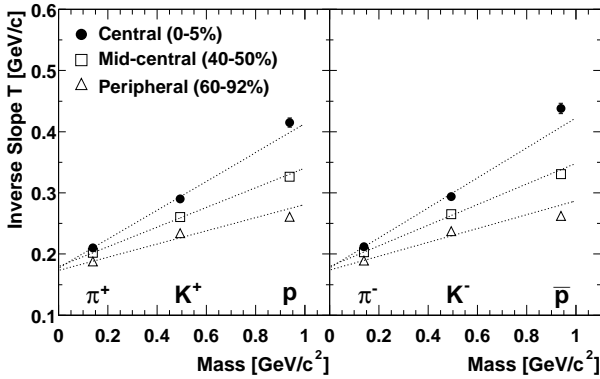


FIG. 17: Mass and centrality dependence of inverse slope parameters T in m_T spectra for positive (left) and negative (right) particles in Au+Au collisions at $\sqrt{s_{NN}} = 200 \text{ GeV}$. The fit ranges are $0.2 - 1.0 \text{ GeV}/c^2$ for pions and $0.1 - 1.0 \text{ GeV}/c^2$ for kaons, protons, and anti-protons in $m_T - m_0$. Figure taken from reference [50].

The detailed study of the higher statistics (anti)proton spectra [50] indicated that (anti)proton spectra cannot be described by a single exponential in $m_T - m_0$, if the full measured range is considered. Although easy to visualize, the one-parameter inverse slope analysis proves to be too simplistic as a way to infer the kinetic properties of the system. In particular, the degree to which the ϕ mesons participate in the collective expansion will be shown (see Fig. 22) to be obscured in this simple approach.

A more sophisticated approach to this problem is to compare the particle spectra to a functional form which describes a boosted thermal source, based on relativis-

tic hydrodynamics [59]. This is a two-parameter model, termed the “blast-wave” model, in which the surface radial flow velocity (β_T) and the freeze-out temperature (T_{fo}) are extracted from the invariant cross section data according to the equation

$$\frac{dN}{m_T dm_T} \propto \int_0^R f(r) r dr m_T I_0\left(\frac{p_T \sinh \rho}{T_{fo}}\right) K_1\left(\frac{m_T \cosh \rho}{T_{fo}}\right), \quad (4)$$

where I_0 and K_1 represent modified Bessel functions with ρ being the transverse boost which depends on the radial position according to

$$\rho = \tanh^{-1}(\beta_T) \cdot r/R \quad (5)$$

Here the parameter R is the maximum radius of the expanding source at freeze-out. The function $f(r)$ represents the density which is taken to be uniform in this calculation.

To study the parameter correlations, we make a grid of (T_{fo}, β_T) pairs and then for each pair we perform a chi-squared minimization for each particle type. We use a linear velocity profile and constant particle density distribution. The first fit attempt is performed simultaneously for the six particle species π^\pm , K^\pm , and the p , \bar{p} in the range $(m_T - m_0) < 1.0 \text{ GeV}/c^2$.

The experimental data for p and \bar{p} have been corrected for Λ and $\bar{\Lambda}$ decays. However, the invariant yields of π^\pm and K^\pm include feed-down from the decay of resonances and weak decays. To take this into account we add the decay of mesonic ($\rho, \eta, \omega, K^* \dots$) and baryonic ($\Delta, \Lambda, \Sigma \dots$) resonances as follows:

- 1) Generate resonances with the transverse momentum distribution determined by each combination of T_{fo} and β_T .
- 2) Simulate the decays using a Monte Carlo approach and obtain π^\pm and K^\pm distributions.
- 3) Merge all particles, where the particle abundance is calculated with chemical parameters [60] $T_{ch} = 177 \text{ MeV}$, $\mu_B = 29 \text{ MeV}$.

The two-parameter T_{fo} vs β_T fit results obtained in this analysis for the most central bin are shown in Fig. 18. Shown in the lower panel of the figure are the χ^2 contour levels obtained from fitting each particle spectrum separately. We observe that the parameters T_{fo} and β_T are anti-correlated, the different particles have different preferred parameter space and different sensitivity to the parameters. For example, the contours for the heavier particles are more sensitive to the flow velocity than to the kinetic freeze-out temperature. The minimum valleys in the contours for the six particle species do overlap at a single common point at the 2σ level. To find the values of the parameters at this overlap point, a simultaneous fit for the six single particle spectra (π^\pm , K^\pm , and p , \bar{p}) was done which converges to a best fit value of

$T_{fo} = 108.9^{+2.6}_{-2.4}$ MeV and $\beta_T = 0.771^{+0.003}_{-0.004}$. Using these parameters, we obtain the transverse momentum shapes shown in Fig. 19 where we also include the prediction for the ϕ spectrum shape which was not part of the original fit. The shape of the ϕ spectrum is reproduced well.

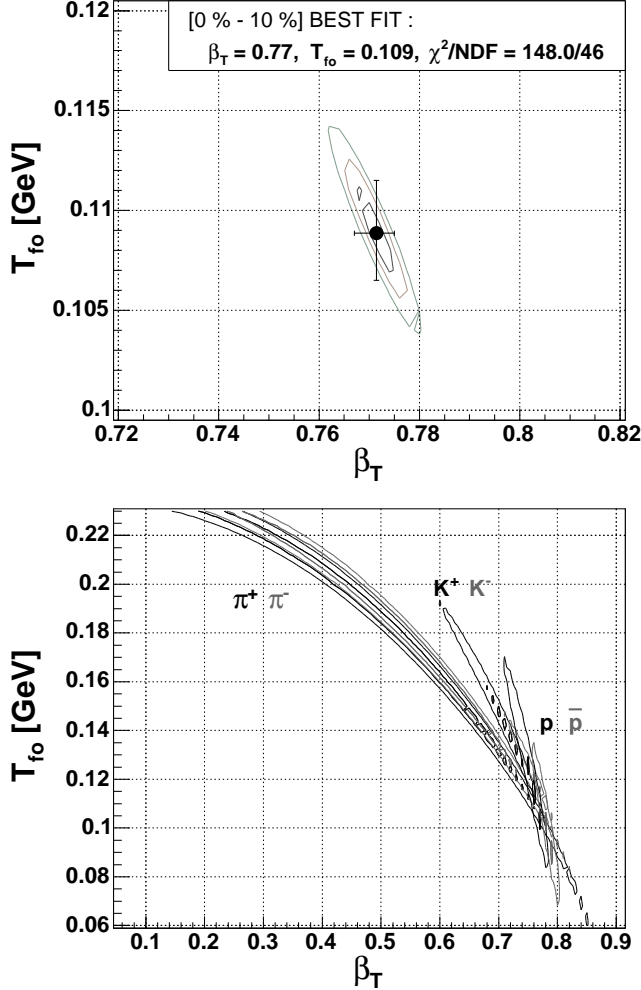


FIG. 18: Contour plots for the hydrodynamical fit to the 200 GeV single particle transverse momentum spectra for the π^\pm , K^\pm , and p, \bar{p} in the 0–10% centrality bin. The contour lines are in one standard deviation steps. The upper plot is from a simultaneous fit with the best value shown as the dot. The lower plot is from independent fits for the six particle spectra.

For the two other centrality bins in this study, 10–40% and 40–92%, we show the best fit hydrodynamical results in Fig. 20 and Fig. 21, respectively. Again we see that the ϕ transverse momentum shapes are reproduced by the same flow parameters which fit the identified hadron data at the same centrality bins.

For a second hydrodynamical fit attempt, we include the ϕ transverse momentum 0–10% centrality data along with the previously identified hadron data as part of the χ^2 minimization search. The flow parameters derived

with the ϕ data included are numerically consistent with the flow parameters derived previously without the ϕ data being included.

The two-dimensional grid search best fit values for the blast-wave parameterization as a function of centrality are tabulated in Table VI. The radial average expansion velocity $\langle \beta_T \rangle$ is also given in this table. For the range of centralities studied here, the expansion velocity parameter is seen to decrease moderately for more peripheral collisions while the kinetic freeze-out temperature increases more significantly, approximately 40%. If one takes these parameters literally, then the more peripheral collisions are subject to decreased radial flow while correspondingly the particles are decoupling kinetically from each other at temperatures closer to the chemical freeze-out temperature. This is a physically reasonable scenario given fewer participants in the initial expansion phase.

It should be pointed out that our present ϕ transverse momentum range does not extend below 0.8 GeV/c. The spectral shapes at low- m_T , especially for the heavier particles, are mostly sensitive to the expansion velocity. In the range of our ϕ measurement, it is more appropriate to consider the asymptotic behavior of the spectral shapes, which for $m_T \gg m_0$ is given by [59]:

$$T_{eff} = T_{fo} \sqrt{(1 + \beta_T)/(1 - \beta_T)} \quad (6)$$

Here, T_{eff} is the slope parameter obtained using m_T exponential fit, as in Eq. (3). It is interesting to note that the measured asymptotic slopes do not seem to depend on centrality, although both T_{fo} and β_T show a clear centrality dependence. This is either due to a cancellation effect in Eq. (6), since the parameters are anti-correlated, or indicates that the hydrodynamics description is no longer valid at these large transverse momenta. We conclude that although the ϕ data themselves cannot constrain the kinematic freeze-out conditions, they are consistent with the hydrodynamical results obtained from the simultaneous fit to the π^\pm , K^\pm , p and \bar{p} spectra.

TABLE VI: Blast wave model parameters [59] as a function of centrality from fitting π^\pm , K^\pm , p and \bar{p} spectra. The fit parameters quoted here are the results from fitting the six identified hadrons spectra simultaneously, without including the ϕ .

Centrality	T_{fo} [MeV]	β_T	$\langle \beta_T \rangle$	χ^2/NDF
0–10%	$108.9^{+2.6}_{-2.4}$	$0.771^{+0.003}_{-0.004}$	$0.572^{+0.003}_{-0.003}$	148.0/46
10–40%	$119.0^{+1.5}_{-1.5}$	$0.748^{+0.003}_{-0.003}$	$0.550^{+0.002}_{-0.002}$	212.1/46
40–92%	150^{+2}_{-2}	$0.630^{+0.005}_{-0.005}$	$0.447^{+0.004}_{-0.004}$	150.9/46

E. Nuclear modification factor R_{CP} for ϕ mesons

One of the most important result demonstrated so far in the study of relativistic heavy ions at RHIC is the

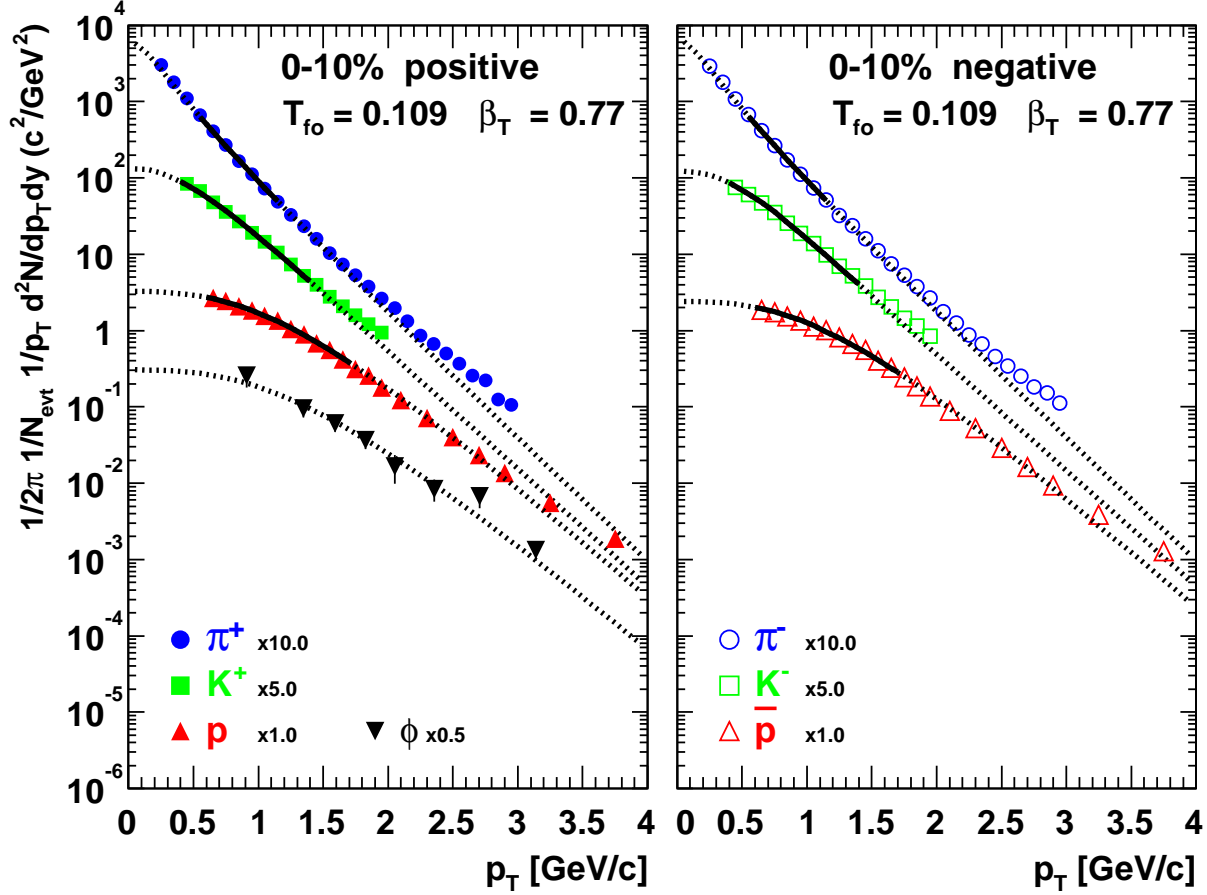


FIG. 19: Transverse momentum data and best fit hydrodynamical results for the 0–10% centrality bin for the 200 GeV π^\pm , K^\pm , and p, \bar{p} , along with the prediction for the ϕ transverse momentum spectrum. The transverse momentum ranges for the fit are indicated by the solid lines, while the dashed lines indicated the extrapolated predictions for each particle species data.

observed suppression of high p_T pions in central collisions as compared to either pp collisions or peripheral Au + Au collisions [62]. A second, quite surprising observation is the unusually large (anti)proton-to-pion ratio at high p_T . In particular PHENIX has observed [30] that in central Au + Au collisions the p/π and \bar{p}/π ratios are enhanced by a factor of 3 at intermediate p_T ($1.5 < p_T < 4.5$ GeV/c) as compared to the ratios in pp collisions and the ratios obtained in quark and gluon jets measured in e^+e^- collisions [61]. It was also observed that proton and anti-proton production scales with N_{coll} in this p_T region, in sharp contrast to the strong suppression of pion production [30]. In pp collisions high p_T particles are the result of the fragmentation of partons. Because of the power law nature of the hard scattering spectrum, most of the particles at high p_T are expected to be leading hadrons. The fragmentation functions, at least in the vacuum, are expected to be universal and independent of the colliding system under consideration. However, at intermediate p_T (1.5–4.5 GeV/c) the PHENIX results from central Au + Au collisions are inconsistent with the

known fragmentation functions.

There are several conjectures which may explain the unexpected PHENIX result:

- 1) hydrodynamic flow generated from the hadronic stage [65], or
- 2) hydrodynamic flow generated at a partonic stage together with particle production from the recombination[32, 33, 34]
- 3) baryon junctions as a mechanism for an usually large build up of baryons and anti-baryons at mid-rapidity [63],
- 4) in-medium modified fragmentation functions [64].

The first three possibilities invoke soft processes to populate a region of p_T that is dominated by hard-scattering in pp collisions. The soft production at intermediate p_T is enhanced for protons and anti-protons, while pions remain dominated by hard-scattering. In

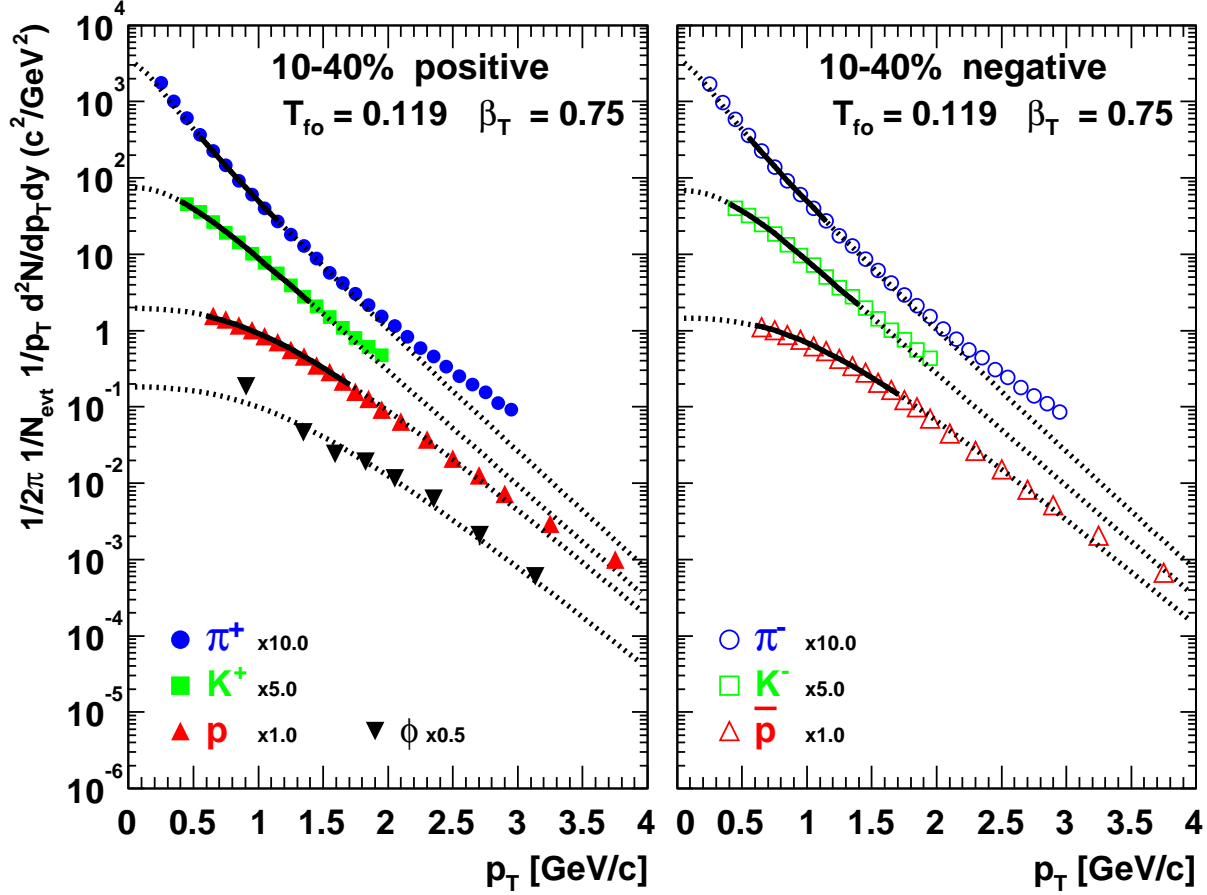


FIG. 20: Transverse momentum data and best fit hydrodynamical results for the 10–40% centrality bin for the 200 GeV π^\pm , K^\pm , and p, \bar{p} , along with the prediction for the ϕ transverse momentum spectrum.

conjecture (4), the production for both pions and p, \bar{p} is by hard-scattering, but the fragmentation functions are modified in the medium, thus resulting in an enhanced p/π and \bar{p}/π ratios.

The second of these conjectures is particularly important since this hypothesis presupposes a partonic state with collective behavior. A critical factor which may differentiate among these scenarios is whether the large abundance of protons is due to its mass, or to the number of constituent valence quarks [32, 33, 34, 35]. Hydrodynamic flow generated at the hadronic stage imparts a single velocity to the moving matter, hence similar mass particles should exhibit the same momentum increase from this effect. In contrast, hypotheses 2 and 3 are dependent on whether the particles are baryons or mesons.

The ϕ meson which has a mass similar to that of a proton yet, like the pion, has two valence quarks, should distinguish between (1) and (2) or (3). We examine the scaling properties of the intermediate p_T yields of the ϕ and compare those to the yields of $(p + \bar{p})/2$. Fig. 22 shows the transverse momentum spectra mea-

sured in three different centralities, each scaled down by the number of binary nucleon-nucleon collisions. The (anti)proton spectra show two pronounced features. Below $p_T < 1.5$ GeV/c, the spectral shapes are strongly influenced by the radial flow and thus the more central data have harder slope. Above $p_T = 1.5$ GeV/c, the effect of radial flow is negligible. The spectra converge to the same line. Moreover, they scale with N_{coll} for all centrality classes, as expected for hard-scattering unaffected by the nuclear medium. The ϕ spectra have a quite different behavior. There is no visible curvature at lower p_T since this curvature is not expected to be prominent in the measured region. At higher p_T the ϕ spectra run parallel to the (anti)proton spectra, but do not obey N_{coll} scaling. To examine this feature on a linear scale, we plot the ratio between the central and peripheral data, *i.e.* the ratio R_{CP} (Fig. 23). The systematic error arising from the determination of N_{coll} is represented by the dotted bar and is about 19%. This systematic error is common for all three particle species shown in the figure. The solid bar around $R_{CP} = 1$ represents the N_{coll} error

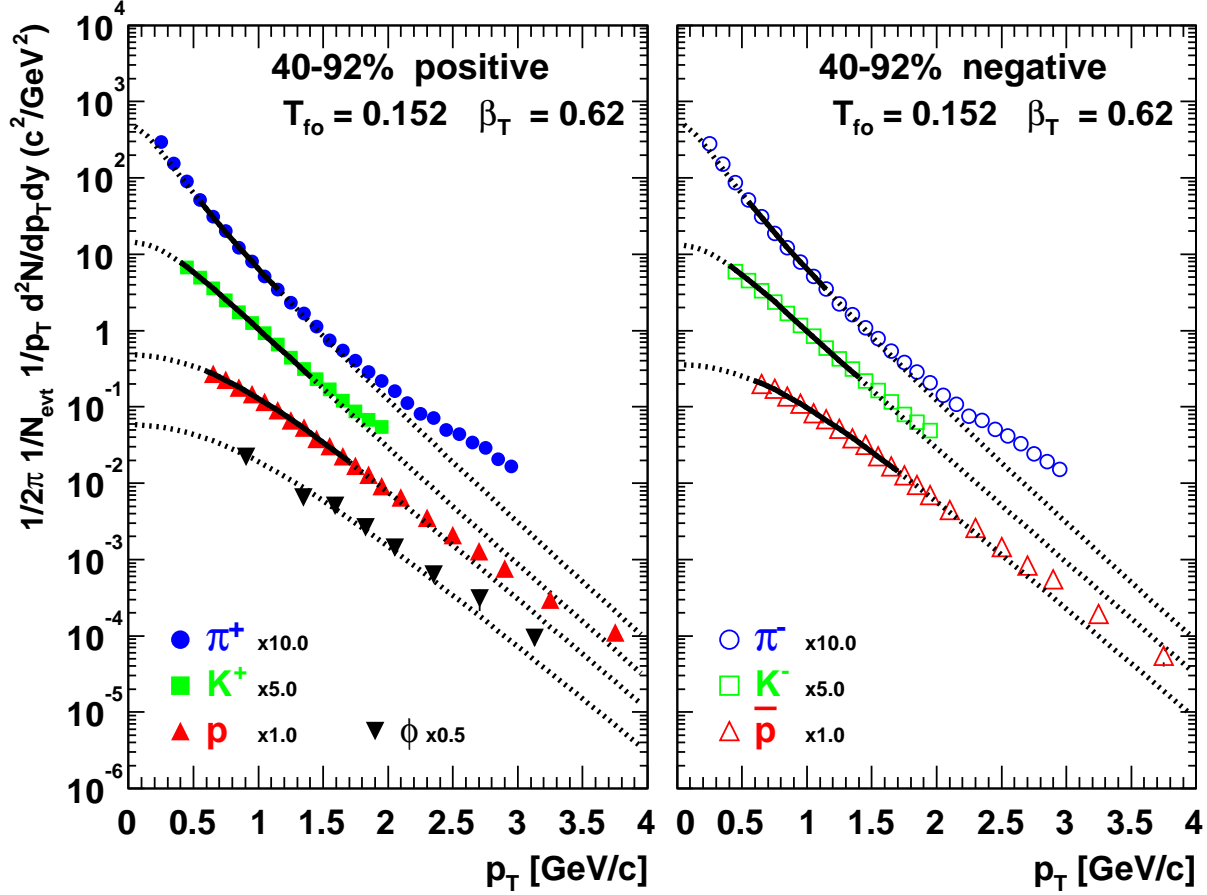


FIG. 21: Transverse momentum data and best fit hydrodynamical results for the 40–92% centrality bin for the 200 GeV π^\pm , K^\pm , and p, \bar{p} , along with the prediction for the ϕ transverse momentum spectrum.

for the protons (the same 19%). Since these errors are correlated, if the curves in the figure were to change due to a change in the value of N_{coll} , they will move together within the extent of the error bars shown. We would like to emphasize the *comparison* between the R_{CP} values for the protons and the ϕ . In this comparison, the systematic errors in determining N_{coll} cancel. The important systematic errors to consider are those that can move the ϕ points with respect to the proton points. When determining a ratio of spectra measured at different centralities, most systematic errors cancel. After removing the N_{coll} error, the sources of error that remain for the ϕ come from the multiplicity dependent corrections and the effect of the mass window as described above. For the protons and pions [29, 30], the error that remains that is independent from the error determined for the ϕ , comes from the multiplicity dependent corrections. The relative error between the ϕ and the proton measurements is evaluated at 7% and is represented by the extended solid bar just below $R_{CP} = 1$. Clearly the ϕ 's behavior is more like that of the pions and not like that of the

protons. Thus we conclude that the ϕ meson exhibits a suppression effect at intermediate p_T similar to that of the pions. Although we can not conclude whether ϕ production at this intermediate p_T is dominated by soft or hard processes, this observation provides support for models which depend on the number of valence quarks in the particle as opposed to models which depend upon just the mass of the particle in order to explain the anomalous proton yields.

V. CONCLUSIONS

A systematic measurement has been made of ϕ production at mid-rapidity in Au+Au collisions with $\sqrt{s_{NN}} = 200$ GeV at RHIC. The general features of the data include the yield which rises from $0.318 \pm 0.028(\text{stat}) \pm 0.051(\text{syst})$ in peripheral collisions to $3.94 \pm 0.60(\text{stat}) \pm 0.62(\text{syst})$ in central collisions. There is seen to be little centrality dependence to the inverse slope which is about 360 MeV. The centroid mass and res-

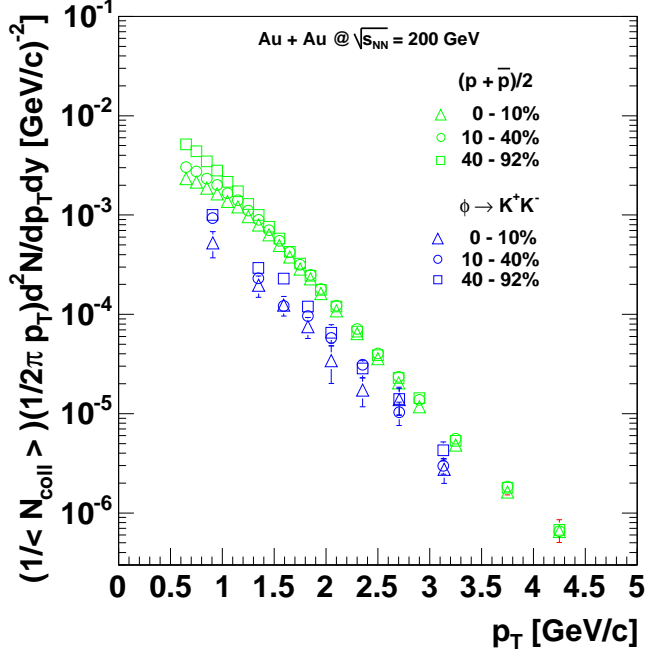


FIG. 22: p_T spectra of proton and ϕ mesons at different centralities scaled down by their respective number of N_{coll}

onance width are extracted with high enough precision to rule out any large (MeV/c^2 scale) deviations from the accepted PDG values. At p_T below $1.5 \text{ GeV}/c$, a blast wave analysis of the most central pion, kaon and proton spectra with a freeze-out temperature T_{fo} of 109 MeV , and a transverse velocity β_T of 0.77 describes the most central ϕ data as well. A similar conclusion, with monotonically changing results for T_{fo} and β_T , holds for the less central events. At higher transverse momenta, all particles lie above the blast wave fits, which suggests that the dominant particle production mechanism is no longer soft physics but is giving way to the expected jet fragmentation. A study of the ratio R_{CP} of the ϕ provides a critical new piece of information in understanding the anomalous proton-to-pion ratio seen in central heavy ion collisions at RHIC, since the ϕ is a meson with a mass similar to that of a proton. The R_{CP} value for the ϕ above a transverse momentum of $1.5 \text{ GeV}/c$ is about 0.6 , similar to that of the pions but inconsistent with the proton value of 1 . This indicates that the ϕ meson is being suppressed in this p_T range for the more central collisions. The lower p_T blast wave fits imply hydrodynamic behavior at the hadronic stage, while the inconsistency with simple hydrodynamics at higher p_T , is something one would expect in the jet fragmentation region. This transition is an important factor to consider as one begins to understand the mechanism of particle production in central collisions at RHIC.

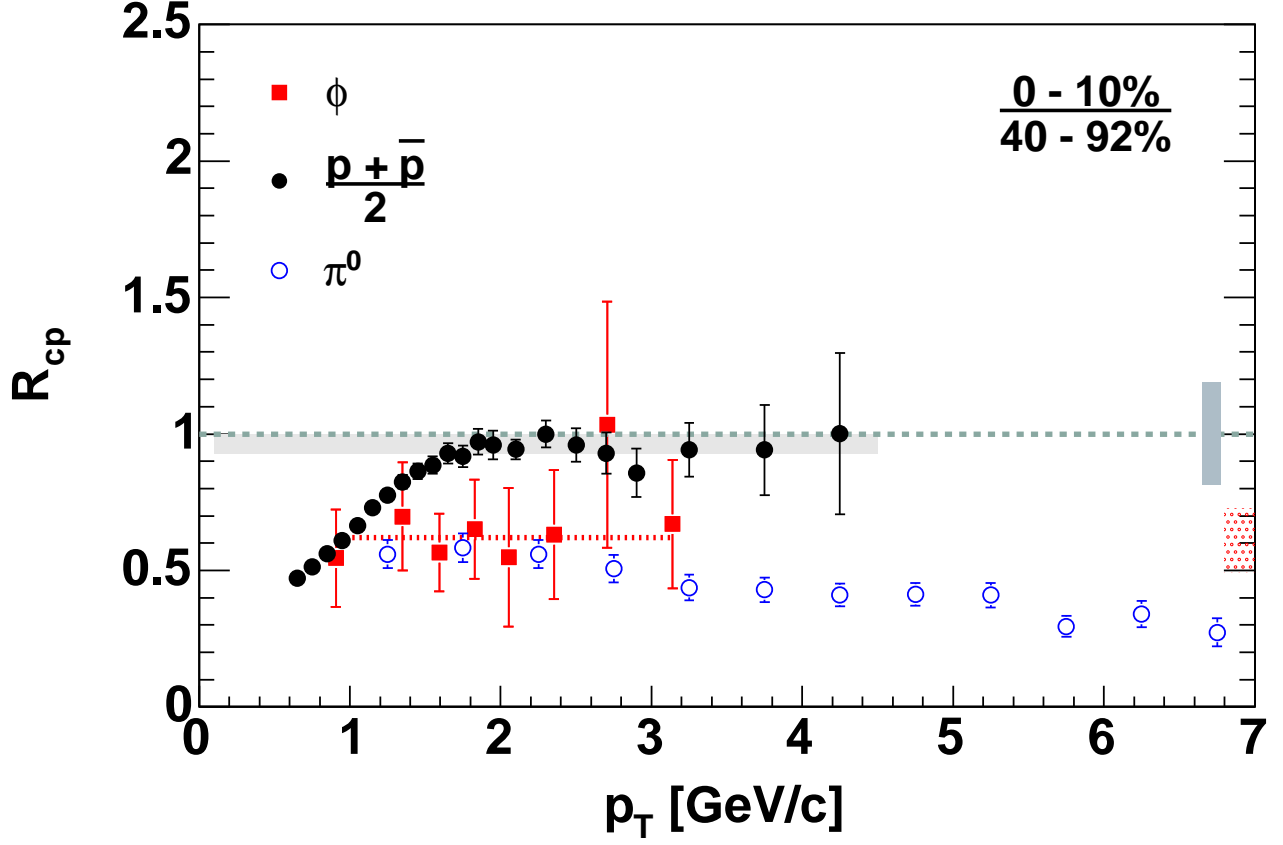


FIG. 23: N_{coll} scaled central to peripheral ratio R_{CP} for $(p + \bar{p})/2$, π^0 , and ϕ . The proton and pion results are published [30]. The vertical dotted bar on the right represents the error on $N_{coll}^{0-10\%}/N_{coll}^{40-92\%}$. The shaded solid bar around $R_{CP} = 1$ represents 12% systematic error which can move the proton and/or ϕ points with respect to one another. The dotted horizontal line at $R_{CP} = 0.62$ is a straight line fit to the ϕ data.

Acknowledgments

We thank the staff of the Collider-Accelerator and Physics Departments at Brookhaven National Laboratory and the staff of the other PHENIX participating institutions for their vital contributions. We acknowledge support from the Department of Energy, Office of Science, Nuclear Physics Division, the National Science Foundation, Abilene Christian University Research Council, Research Foundation of SUNY, and Dean of the College of Arts and Sciences, Vanderbilt University (U.S.A), Ministry of Education, Culture, Sports, Science, and Technology and the Japan Society for the Promotion of Science (Japan), Conselho Nacional de Desenvolvimento Científico e Tecnológico and Fundação de Amparo à Pesquisa do Estado de São Paulo (Brazil), Natural Science Foundation of China (People's Republic of China), Centre National de la Recherche Scientifique, Commissariat à l'Énergie Atomique, Institut National de Physique Nucléaire et de Physique des Particules, and Institut National de Physique Nucléaire et de Physique des Particules, (France), Bundesministerium für Bildung und Forschung, Deutscher Akademischer Austausch Dienst, and Alexander von Humboldt Stiftung (Germany), Hungarian National Science Fund, OTKA (Hungary), Department of Atomic Energy and Department of Science and Technology (India), Israel Science Foundation (Israel), Korea Research Foundation and Center for High Energy Physics (Korea), Russian Ministry of Industry, Science and Technologies, Russian Academy of Science, Russian Ministry of Atomic Energy (Russia), VR and the Wallenberg Foundation (Sweden), the U.S. Civilian Research and Development Foundation for the Independent States of the Former Soviet Union, the US-Hungarian NSF-OTKA-MTA, the US-Israel Binational Science Foundation, and the 5th European Union TMR Marie-Curie Programme.

APPENDIX A: COMBINATORIAL BACKGROUND

Assume there are N tracks per event of which n are positive and $N-n$ are negative, the probability of the partition being $P(n)$ such that $\sum_{n=0}^N P(n) = 1$.

All expressions below refer to the average number of pairs per event

1. General relation between the number of like and unlike pairs

The total number of pairs is:

$$N_{pairs} = \frac{N(N-1)}{2} \quad (A1)$$

The number of + - pairs is:

$$n_{+-} = \sum_{n=0}^N n(N-n)P(n) = N\langle n \rangle - \langle n^2 \rangle \quad (A2)$$

The number of + + pairs is:

$$n_{++} = \sum_{n=0}^N \frac{n(n-1)}{2} P(n) = \frac{\langle n^2 \rangle - \langle n \rangle}{2} \quad (A3)$$

The number of - - pairs is:

$$n_{--} = \sum_{n=0}^N \frac{(N-n)(N-n-1)}{2} P(n) \quad (A4)$$

$$n_{--} = \frac{N(N-1)}{2} - (N - \frac{1}{2})\langle n \rangle + \langle n^2 \rangle \quad (A5)$$

We therefore get:

$$n_{++} + n_{--} = \frac{N(N-1)}{2} - (N\langle n \rangle - \langle n^2 \rangle) \quad (A6)$$

The last expression is trivial: the number of like-sign pairs is equal to the total number pairs minus the number of unlike-sign pairs.

The ratio R of unlike to like pairs is therefore:

$$R = \frac{n_{+-}}{n_{++} + n_{--}} = \frac{N\langle n \rangle - \langle n^2 \rangle}{N(N-1)/2 - (N\langle n \rangle - \langle n^2 \rangle)} \quad (A7)$$

This is a general result, free of any assumption and should always be fulfilled, in pure combinatorial background as well as in a mixture of signal + combinatorial background.

2. Combinatorial background

Consider a pure combinatorial background sample. By its essence there are no correlations between tracks in such a sample i.e. within an event the probability p to have a positive (or a negative) track is constant and independent of the number of tracks. Therefore the probability $P(n)$ of having n positive tracks out of the total of N tracks is given by a binomial distribution:

$$P(n) = \frac{N!}{n!(N-n)!} p^n (1-p)^{N-n} \quad (A8)$$

$$\langle n \rangle = pN \quad (A9)$$

$$\langle n^2 \rangle = \sigma^2 + \langle n \rangle^2 = Np(1-p) + p^2 N^2 \quad (A10)$$

Replacing these values in expression (6) gives:

$$R = \frac{(p - p^2)}{(1/2 - p + p^2)} \quad (\text{A11})$$

If there is charge symmetry, i.e. $p = 0.5$ one gets $R = 1$ and consequently the combinatorial background is given by:

$$n_{+-}^{CB} = n_{++} + n_{--} \quad (\text{A12})$$

This is an exact relation. It holds with quite good accuracy even if there is some charge asymmetry. For example for an asymmetry of 10% (i.e. $p = 0.525$) $R=0.995$.

3. The formula $N_{+-}^{CB} = 2\sqrt{N_{++}N_{--}}$

The combinatorial background is rigorously given by this formula provided that the number N of tracks per event has a Poisson distribution:

$$\mathcal{P}(N) = \frac{\langle N \rangle^N e^{-N}}{N!} \quad (\text{A13})$$

Again we assume that the N tracks are divided into n positive and $(N-n)$ negative tracks, the partition is given by the binomial distribution (A7) and all expressions below refer to average number of pairs per event. Number of $++$ pairs:

$$N_{++} = \sum_{N=2}^{\infty} \mathcal{P}(N) \sum_{n=0}^N P(n) \frac{n(n-1)}{2} \quad (\text{A14})$$

Using relations (A7) and (A11) and some algebra leads to:

$$N_{++} = \frac{1}{2} p^2 \langle N \rangle^2 \quad (\text{A15})$$

Similarly the number of $--$ pairs is given by:

$$N_{--} = \sum_{N=2}^{\infty} \mathcal{P}(N) \sum_{n=0}^N P(n) \frac{(N-n)(N-n-1)}{2} \quad (\text{A16})$$

$$= \frac{1}{2} (1-p)^2 \langle N \rangle^2 \quad (\text{A17})$$

The number of combinatorial background $+-$ pairs is:

$$N_{+-}^{CB} = \sum_{N=2}^{\infty} \mathcal{P}(N) \sum_{n=0}^N P(n) n(N-n) \quad (\text{A18})$$

$$= p(1-p) \langle N^2 \rangle \quad (\text{A19})$$

Inspecting (A15), (A16) and (A17) shows that:

$$N_{+-}^{CB} = 2\sqrt{N_{++}N_{--}} \quad (\text{A20})$$

APPENDIX B: DATA TABLES OF CENTRALITY SELECTED ϕ SPECTRA

The invariant yields, $\frac{1}{2\pi m_T} \cdot \frac{d^2 N}{dm_T dy}$, of the ϕ mesons in different centrality bins are shown in Table VII.

APPENDIX C: SYSTEMATIC ERRORS ON dN/dy AND T

The sources of the systematic errors on yield (dN/dy and T) measurements are as follows:

a) Systematic error on the combinatorial background normalization, δ_{norm} : This originates from the systematics of the event mixing. Since both same event and mixed event like sign distributions represent pure combinatorials, we estimated unlike sign combinatorial background by normalizing the mixed event unlike sign distributions to $2\sqrt{N_{++}^{Same event} \cdot N_{--}^{Same event}}$ and $2\sqrt{N_{++}^{Mixed event} \cdot N_{--}^{Mixed event}}$ and the difference in the extracted ϕ signal from the real data between these two normalizations are attributed as the systematic uncertainty.

We use the same normalization factor for all m_T bins. So, the above systematics are applicable to the measured dN/dy only, not on the inverse slope, T .

b) Systematics of ϕ mass window, δ_{mass} : We count the number of reconstructed ϕ mesons by integrating the ϕ meson invariant mass spectra within ± 5 MeV mass window with respect to the measured centroids in both data and Monte Carlo. The systematic associated with this mass window is estimated by measuring the extent of the changes in dN/dy and T after constructing ϕ meson m_T spectra within five different mass windows $\pm 3, \pm 5, \pm 8, \pm 10$ and ± 15 MeV, with respect to the measured ϕ centroids.

c) Uncertainties in extrapolation of ϕ meson m_T spectra to $m_T = m_\phi$, δ_{extrap} : This is studied by (i) fitting the m_T distributions using exponential and Boltzmann functions. two different fitting functions, exponential and Boltzmann, and (ii) fitting the transverse mass spectra within different m_T ranges. These are applied to both dN/dy and T .

d) Acceptance correction systematics, δ_{MC} : The systematics associated with acceptance correction factors derived from Monte Carlo analysis are investigated by considering two sources:

- (i) Tuning of detector alignments in Monte Carlo with reference to the real data ($\sim 3\%$), and
- (ii) Systematics in the fiducial geometries in data and Monte Carlo ($\sim 12\%$).

The systematic error from this source is independent of the momenta of reconstructed ϕ mesons. So, this is attributed to dN/dy only.

TABLE VII: m_T spectra of ϕ mesons in different centrality bins. The systematic errors on invariant yields are from combinatorial background normalization, ϕ counting mass window, acceptance correction efficiencies from Monte Carlo and occupancy dependent corrections.

Centrality (%)	m_T (GeV/ c^2)	m_T bin size (GeV/ c^2)	$\frac{1}{2\pi m_T} \frac{d^2 N}{[(GeV^2/c^4)^{-2}]}$	Stat. error [(GeV $^2/c^4$) $^{-2}$]	Syst. error [(GeV $^2/c^4$) $^{-2}$]
0 - 10	1.365	0.4	0.51114	0.15120	0.0778747
	1.691	0.2	0.19114	0.04656	0.029121
	1.891	0.2	0.12065	0.02702	0.018382
	2.091	0.2	0.07313	0.01758	0.011142
	2.291	0.2	0.03335	0.01372	0.005081
	2.565	0.4	0.01683	0.00541	0.002564
	2.891	0.2	0.01353	0.00406	0.002061
	3.300	1.0	0.00268	0.00074	0.000408
10 - 40	1.364	0.4	0.37232	0.04145	0.05667
	1.691	0.2	0.09224	0.01255	0.01404
	1.891	0.2	0.04872	0.00719	0.00742
	2.091	0.2	0.03867	0.00483	0.00589
	2.291	0.2	0.02320	0.00389	0.00353
	2.564	0.4	0.01246	0.00160	0.00189
	2.891	0.2	0.00415	0.00110	0.00063
	3.294	1.0	0.00120	0.00021	0.00018
40 - 92	1.364	0.4	0.04432	0.00622	0.00645
	1.691	0.2	0.01295	0.00185	0.00189
	1.891	0.2	0.01009	0.00110	0.00147
	2.091	0.2	0.00531	0.00074	0.00077
	2.291	0.2	0.00287	0.00060	0.00042
	2.563	0.4	0.00126	0.00024	0.00018
	2.891	0.2	0.00062	0.00019	0.00009
	3.293	1.0	0.00019	0.00004	0.00003

TABLE VIII: Systematic error in dN/dy .

Centrality (%)	δ_{norm} (%)	δ_{mass} (%)	δ_{extrap} (%)	δ_{MC} (%)	δ_{occu} (%)	δ_{sys}^{tot} (%)
Minimum Bias	0.7	2.6	4.0	12.4	7.8	15
0 - 10	0.8	4.2	5.2	12.4	10	17
10 - 40	1.1	2.3	5.9	12.4	8.5	16
40 - 92	0.7	3.1	6.0	12.4	7	16

TABLE IX: Systematic error in T .

Centrality (%)	δ_{mass} (%)	δ_{fit} (%)	δ_{sys}^{tot} (%)
Minimum Bias	0.6	4.9	5
0 - 10	1.1	5.2	5
10 - 40	1.1	6.2	6
40 - 92	1.1	4.2	4

e) Systematic error in the occupancy dependent efficiency corrections, δ_{occu} : The systematic error associated with this efficiency is estimated by calculating the occupancy dependent correction with different track confirmation criteria and is independent of the pair momenta. This is a systematic effect on dN/dy only.

The above systematic errors are quoted in Tables VIII and IX for dN/dy and T , respectively.

-
- [1] See E. Laermann and O. Philipsen, hep-ph/0303042 (to appear in Ann. Rev. Nuc. Part. Sc.) for a recent review.
- [2] J. D. Bjorken, Phys. Rev. **D27**, 140 (1983).
- [3] PHENIX Collaboration, K. Adcox *et al.*, Phys. Rev. Lett. **87**, 052301 (2001).
- [4] J. Rafelski and B. Müller, Phys. Rev. Lett. **48**, 1066 (1982).
- [5] A. Shor, Phys. Rev. Lett. **54**, 1122 (1985).
- [6] P. Koch, B. Müller, and J. Rafelski, Phys. Rep. **142**, 167 (1986).
- [7] C. P. Singh, Phys. Rev. Lett. **56**, 1750 (1986).
- [8] C. P. Singh, Phys. Lett. **B188**, 369 (1987).
- [9] C. P. Singh, Phys. Rep. **236**, 147 (1993).
- [10] C. P. Singh, *et al.*, Phys. Lett. **B393**, 188 (1997).
- [11] S. A. Bass *et al.*, Nucl. Phys. **A661**, 205 (1999).
- [12] J.-P. Blaizot and R. Mendez Galain, Phys. Lett. **B271**, 32 (1991).
- [13] S. Pal, C.M. Ko, and Z. Lin, Nucl. Phys. **A707**, 525 (2002).
- [14] P. Bi and J. Rafelski, Phys. Lett. **B262**, 485 (1991).
- [15] M. Asakawa and C.M. Ko, Nucl. Phys. **A572**, 732 (1994).
- [16] C. Song, Phys. Lett. **B388**, 141 (1996).
- [17] M. Asakawa and C.M. Ko, Phys. Lett. **B322**, 33 (1994).
- [18] C. M. Ko and D. Seibert, Phys. Rev. **C49**, 2198 (1994).
- [19] K. Haglin, Nucl. Phys. **A584**, 719 (1995).
- [20] W. Smith and K.L. Haglin, Phys. Rev. **C57**, 1449 (1998).
- [21] E. Oset and A. Ramos, Nucl. Phys. **A679**, 616 (2001).
- [22] S. Okubo, Phys. Lett. **B5**, 165 (1963).
- [23] D. Cabrera and M.J. Vicente Vacas, Phys. Rev. **C67**, 045203 (2003).
- [24] S. Eidelman *et al.*, Phys. Lett. **B592**, 11 (2004).
- [25] B. Alessandro *et al.*, Phys. Lett. **B555**, 147 (2003).
- [26] V. Friese *et al.*, Nucl. Phys. **A698**, 487 (2002).
- [27] PHENIX Collaboration, K. Adcox *et al.*, Phys. Rev. Lett. **88**, 022301 (2002).
- [28] PHENIX Collaboration, K. Adcox *et al.*, Phys. Lett. **B561**, 82 (2003).
- [29] PHENIX Collaboration, S. S. Adler *et al.*, Phys. Rev. Lett. **91**, 072303 (2003).
- [30] PHENIX Collaboration, S. S. Adler *et al.*, Phys. Rev. Lett. **91**, 172301 (2003).
- [31] PHENIX Collaboration, K. Adcox *et al.*, Phys. Rev. Lett. **88**, 242301 (2002).
- [32] R. J. Fries, B. Müller, C. Nonaka and S. A. Bass, Phys. Rev. C **68**, 044902 (2003) [arXiv:nucl-th/0306027]; R. J. Fries, B. Müller, C. Nonaka and S. A. Bass, Phys. Rev. Lett. **90**, 202303 (2003) [arXiv:nucl-th/0301087].
- [33] R. C. Hwa and C. B. Yang, arXiv:nucl-th/0401001;
- [34] V. Greco, C. M. Ko and P. Lévai, “Parton coalescence at RHIC,” Phys. Rev. C **68**, 034904 (2003) [arXiv:nucl-th/0305024].
- [35] V. Greco, C. M. Ko and P. Lévai, Phys. Rev. Lett. **90**, 202302 (2003) [arXiv:nucl-th/0301093].
- [36] Y. Akiba *et al.*, Phys. Rev. Lett. **76**, 2021 (1996).
- [37] H. Fesefeldt *et al.*, Nucl. Phys. **B147**, 317 (1979); D. Drijard *et al.* Z. Phys. **C9**, 293 (1981), and references therein.
- [38] E917 Collaboration, B. B. Back *et al.*, Phys. Rev. **C69**, 054901 (2004).
- [39] NA49 Collaboration, S.V. Afanasiev *et al.*, Phys. Lett. **B491**, 59 (2000).
- [40] NA38 Collaboration, M. C. Abreu *et al.*, Phys. Lett. **B368**, 239 (1996).
- [41] NA50 Collaboration, M. C. Abreu *et al.*, Phys. Lett. **B555**, 147 (2003); Erratum - *ibid.* B561:294,2003.
- [42] D. Rohrich *et al.*, Journ. Phys. G **27** (2001) 355
- [43] STAR Collaboration, C. Adler *et al.*, Phys. Rev. **C65**, 041901R (2002).
- [44] PHENIX Collaboration, K. Adcox *et al.*, Nucl. Instrum. Methods **A499**, 469 (2003).
- [45] PHENIX Collaboration, M. Aizawa *et al.*, Nucl. Instrum. Methods **A499**, 508 (2003).
- [46] PHENIX Collaboration, L. Aphecetche *et al.*, Nucl. Instrum. Methods **A499**, 521 (2003).
- [47] PHENIX Collaboration, M. Allen *et al.*, Nucl. Instrum. Methods **A499**, 549 (2003).
- [48] PHENIX Collaboration, C. Adler *et al.*, Nucl. Instrum. Methods **A470**, 488 (2001).
- [49] PHENIX Collaboration, K. Adcox *et al.*, Nucl. Instrum. Methods **A499**, 489 (2003).
- [50] PHENIX Collaboration, S. S. Adler *et al.*, Phys. Rev. **C69**, 034909 (2004)
- [51] J. T. Mitchell *et al.*, Nucl. Instrum. Methods **A482**, 491 (2002).
- [52] L. Aphecetche *et al.*, Nucl. Instrum. Methods **A499**, 521 (2003).
- [53] GEANT 3.21, CERN program library.
- [54] F. Klingl, T. Waas, and W. Weise, Phys. Lett. **B431**, 254 (1998).
- [55] R. Rapp and J. Wambach, Adv. Nucl. Phys. **25**, 1 (2000).
- [56] L. Alvarez-Ruso and V. Koch, Phys. Rev. **C65**, 054901 (2002).
- [57] NA44 Collaboration, Phys. Rev. Letters **78** (1997) 2080; Phys. Rev. C **59** (1999) 328; Phys. Letters B **388** (1996) 431; Phys. Rev. C **57** (1998) 837.
- [58] WA97 Collaboration, E. Andersen *et al.*, Journ. Phys. G **25** (1999) 171.
- [59] E. Schnedermann, J. Sollfrank, and U. Heinz, Phys. Rev. C **48**, 2462 (1993).
- [60] P. Braun-Munzinger, D. Magestro, K. Redlich, and J. Stachel, Phys. Lett. B **518**, 41, (2001).
- [61] DELPHI Collaboration, P. Abreu *et al.*, Eur. Phys. J. **C17**, 207 (2000).
- [62] PHENIX Collaboration, S. Adler *et al.*, Phys. Rev. **C69**, 034910 (2004).
- [63] G.C. Rossi and G. Veneziano, Nucl. Phys. **B123**, 507 (1977); D. Kharzeev, Phys. Lett. **B378**, 238 (1996); S.E. Vance, M. Gyulassy, X.-N. Wang, Phys. Lett. **B443**, 45 (1998); I. Vitev and M. Gyulassy, Phys. Rev. **C65**, 041902 (2002)
- [64] X.-N. Wang, NPA **702**, 238 (2002).
- [65] T. Hirano and Y. Nara, [arXiv:nucl-th/0404039]; T. Hirano and K. Tsuda, PRC **66**, 054905 (2002); D. Teaney, J. Lauret and E. V. Shuryak, Phys. Rev. Lett. **86**, 4783 (2001); P. Kolb *et al.*, Nucl. Phys. **A696**, 197 (2001); P. Huovinen *et al.*, Phys. Lett. **B503**, 58 (2001).
- [66] J. Adams *et al.*, [arXiv:nucl-ex/0406003].